First Contact: Fine Structure of the Impact Flash and Ejecta during Hypervelocity Impact

Gary Simpson[a,b], Matthew Shaeffer[b], Justin Moreno,[b] and K.T. Ramesh[a,b,*]

a - Department of Mechanical Engineering, Johns Hopkins University, Baltimore, MD 21218, USA

b - Hopkins Extreme Materials Institute, Johns Hopkins University, Baltimore, MD 21218, USA

* - Corresponding Author, Email: ramesh@jhu.edu

Abstract

Hypervelocity impacts are a major threat in low-earth orbit and in hypersonic applications. The mechanisms activated under these extreme conditions are typically obscured by a very bright flash, called the impact flash, that contains within it the signatures of the critical mechanisms, the impacting materials, and the impact environment. However, these signatures have been very difficult to observe because of the small length and time scales involved coupled with the high intensities associated with the flash. Here we perform experiments investigating the structure and characteristics of the impact flash using unprecedented temporally co-registered high-resolution diagnostics. Reciprocal impact configurations, in which the projectile and target material are swapped, are used to demonstrate the coupling of early-stage mechanisms in the flash and later-stage ejection mechanisms responsible for the development of the impact crater.

1 Introduction and Background

Hypervelocity impact occurs in critical applications ranging from hypersonic aircraft transiting dusty atmospheres to micrometeoroids impacting orbiting satellites (Figure 1). Such impacts generate a short but intense emission of electromagnetic (EM) radiation that is referred to as the impact flash. The wavelengths in the flash can range from radio frequencies (RF) to ultraviolet (UV). Both wavelength and intensity vary greatly with impact conditions and environment, indicating a coupling between the impact-induced mechanisms and the EM signature. The intense flash often prevents optical observation of the earliest moments of projectile contact and target penetration. However, the flash also contains important information on the highest energy processes occurring during first contact, and understanding this signature is very valuable in planetary, aerospace, and national security applications.

The earliest phase (first contact) of projectile/target interaction in hypervelocity impacts is extremely difficult to access with time-resolved in-situ methods. The connections between early mechanisms (such as impact jetting) and the later-stage mechanisms of deformation and failure have therefore been difficult to determine. For the purposes of this manuscript, we define the early phase mechanisms as those occurring within the time-scale $\tau = \frac{V_0}{r_i}$, where V_0 is the impact velocity and r_i is the radius of the spherical impactor. We further define late-stage mechanisms as those developed at times greater than 5τ. A better understanding of how the initial impact mechanisms evolve and then connect to the late-stage mechanisms responsible for crater growth and large scale material ejection is critical to applications such as hypersonics. For example, at hypersonic velocities (Mach number $M \geq 5$) particle impacts can create substantial damage, alter surface characteristics, and create energetic mixed-phase flows within the boundary layer, degrading control surfaces and disrupting critical aerodynamic gas flows near the impacted surface[1]. Here we use direct time-resolved and in situ experimental methods to examine both the early stage and the later stage mechanisms.

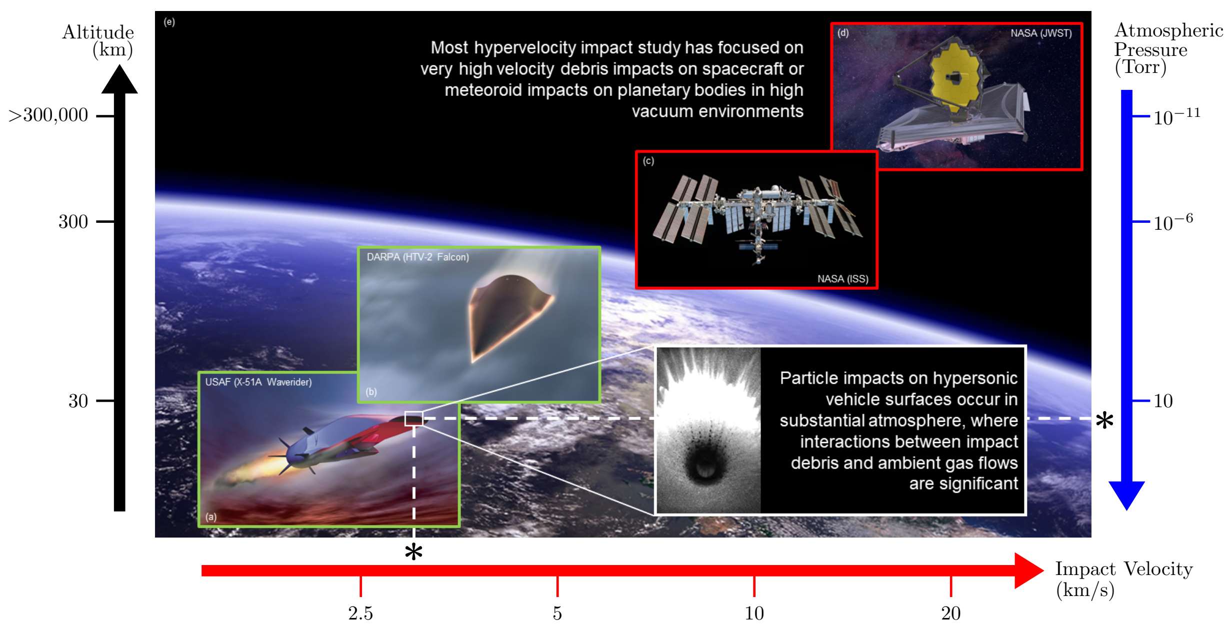

Figure 1: Hypervelocity impacts occur in a wide range of aerospace and planetary applications, with a range of impact velocities and ambient atmospheres. The experimental conditions investigated in this work, for example, are equivalent to the ambient atmospheric density at an altitude of approximately 30 km (relevant to the upper and lower operational envelopes of hypersonic air-breathing and boost-glide vehicles respectively). Background images: (a)[2], (b)[3], (c)[4], (d)[5], (e)[6].

Prior experimental studies of high velocity impact flash revealed a variety of behaviors,[7–11]in terms of the evolution of the total flash intensity with time. At high impact velocities in high vacuum environments, the history of the flash intensity shows two[10,12] or three[11,13] regimes: an initial sub-microsecond duration "spike" in intensity (often attributed to impact jetting[10,13–15]), a long duration "tail" (previously attributed to ejecta ablation[13,16]), and occasionally an intermediate peak (attributed to shock-induced vaporization[13]). Material-atmosphere interactions may also have dramatic effects on the impact flash.[17,18]

A number of experimental investigations of the spectral content of the impact flash have been performed[14,18–21] at high impact velocities (5-7 $km\ s^{-1}$). At impact velocities in excess of 10 $km\ s^{-1}$ projectiles may be shock vaporized entirely, and the radiation dynamics and expansion of the vapor and plasma dominate the impact flash[22,23]. Kadono and Fujiwara[24] imaged the expansion of impact vapor clouds under such conditions, using nylon projectiles (which vaporize at lower velocities). Other works have examined the chemistry and evolution of impact vapor clouds[12,25–28] at late times by combining imaging and spectroscopy. Mihaly et al[27,28] investigated impact flash using nylon cylinders impacting aluminum targets at approximately 6 $km\ s^{-1}$, conditions in which near total vaporization of the projectile would be expected,[24] but their experimental configuration prevented imaging, spectroscopic, or photometric observations before 3 μs after initial impact (equivalent to $\sim 20\tau$).

At impact velocities of $\leq 5\ km\ s^{-1}$ with metals, there is typically insufficient energy to directly vaporize material. However, strong atomic and ionic gas phase characteristic radiation is observed during prompt emission at modest impact velocities, indicating temperatures in excess of those expected from plane shock compression. Here we investigate the flash behavior at such velocities in structural metals, examining the early-stage mechanisms of projectile-target interaction and their role in the production of energetic, radiating material. We also investigate the evolution of the early phase ejection and flash phenomena and the mechanistic transition to the later-stage development of the familiar ejecta cone. We provide direct experimental observations of impact jetting and flash behavior in reciprocal projectile/target systems (necessary to separate material and geometry effects on the jetting mechanism). Impact jetting[15,29,30] is a mechanism that has received considerable attention in the planetary science community as a viable melt generating mechanism.[31]

2 Results and Discussion

The impact of a 5 mm diameter sphere made of 304 stainless steel (304SS) into a 6061-T6 Al alloy target plate at an impact velocity of 3 $km\ s^{-1}$ is shown in Fig. 2. In this case the characteristic timescale is $\tau = 0.8\ \mu s = 800\ ns$. Figures 2a-f show a selection of high-speed camera images taken over the first few μs after impact, with each image pair showing the side view on the left and the front view on the right.

The impact flash is first observed as an intensely bright disk within 200 ns after contact (Fig. 2a), with the impactor still visible. The bright disk-shaped zone grows over the next 800 ns, and begins to show (Fig. 2b) some structure. The center of the impact crater is just visible in the front view of Fig. 2c. In Fig. 2d, the side view of the bright zone shows two distinct components, a bright inner zone and a faster-moving, less intense outer zone. The component farther away from the target plate is expanding (radially) faster than is the inner component. At this time the radial periphery of the outer component shows signs of radial structure. Just over 3 μs later, looking at the side view of Fig. 2e, the outer component shows all of the characteristics of the classical ejecta cone, with dark ejecta particles in the cone; the inner component now shows perceptible bright blobs, while the outer component is now difficult to see in the front view. The outer parts of the darker ejecta cone smoothly transition into the edge of the outer zone, suggesting trajectory continuity between the ejected material forming the outer component and the material in the ejecta cone. By the time of Fig. 2f, 13.4 μs after impact, the inner component is cooling and dissipating with radial fingers propagating slowly at the radial edge. The outer emission zone has dimmed as well, and is just perceptible towards the right edge of the image frame; the full extent of the ejecta cone is now visible. Note that the target plate has been fully perforated at this time.

The outer emission zone in Figs. 2d-f is brightest along the uprange direction and very faint along the target plate surface as it expands. The streak like appearance of the outer zone front in Figs. 2d-e indicates that this zone contains condensed particles. In contrast, the inner emission zone in Figs. 2d-f is bright both along the target surface and along the impact direction (uprange), consistent with an expanding vapor cloud (e.g., Kadono and Fujiwara[24]). The front view in Figure 2e shows that the circumference of the inner zone has now developed radial finger-like structures, instabilities resulting from the interaction of the vapor cloud with the ambient atmosphere[32]. The corresponding evolution of the visual (VIS) and near infrared (NIR) luminosities are shown in Fig. 2g, with the times corresponding to each of the high-speed camera images noted in Figure 2a-f. The peak in NIR intensity occurs just before the time corresponding to Fig. 2c, while the VIS luminosity peaks at 1.8 μs, corresponding to Fig. 2c. Both curves decay thereafter over about 15 μs, during the times corresponding to Figs. 2d-f. The luminosity data is spatially integrated over a larger field of view than shown in these images, and so the observed decay is not due to material leaving the field of view. The cavity generated by the impact no longer expands after about 10 μs post impact (i.e., new ejecta are not being added after this time).

Figure 2h shows short exposure UV/VIS gated spectra obtained during the flash event; two separate spectra are obtained over the time-windows (exposures) marked #1 and #2 in Fig. 2g (one obtained just before the VIS luminosity peak, and the other well after). Both spectra are dominated by characteristic emission. The most intense characteristic emissions observed are Al I atomic peaks[33] as indicated on the

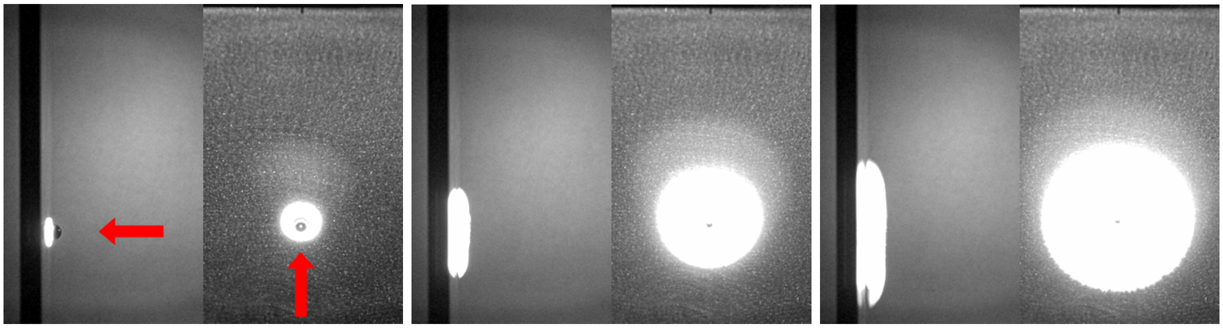

(a) $t = 0.2\,\mu s$ (b) $t = 1.0\,\mu s$ (c) $t = 1.8\,\mu s$

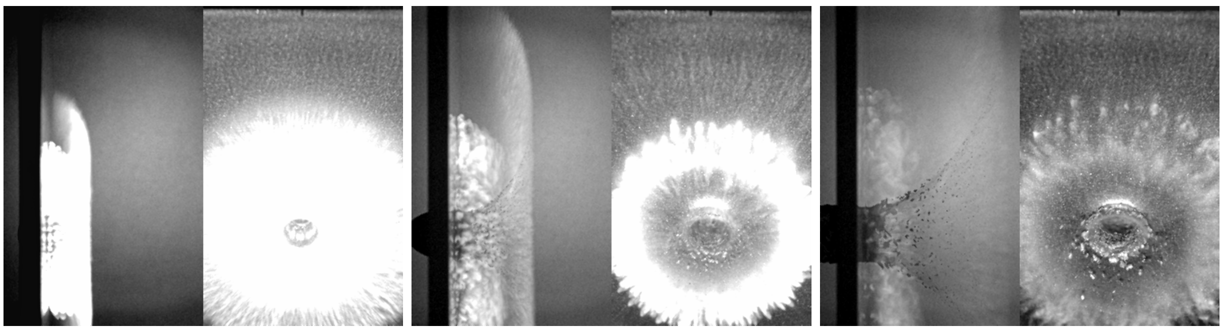

(d) $t = 4.0\,\mu s$ (e) $t = 7.4\,\mu s$ (f) $t = 13.4\,\mu s$

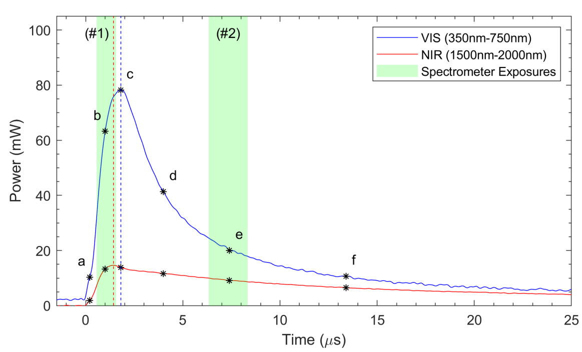

(g) Visual and Near-IR Luminosity

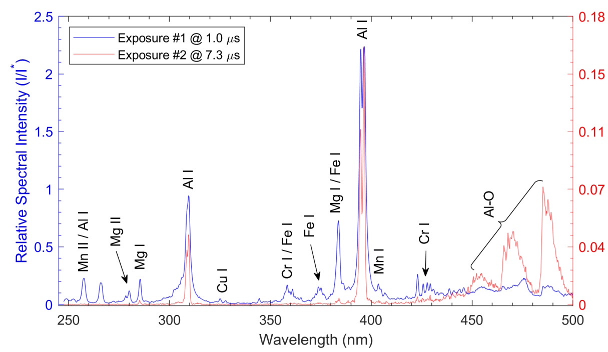

(h) UV-Visual Gated Spectra (250-500nm)

Figure 2: 304SS projectile impacting 6061Al target at 90°obliquity with velocity of 3.0 km/s in 15 Torr air. Selected images, (a)-(f) are shown as time-matched pairs with both side camera (left image) and front camera (right image) views. Exposure time is 110 ns for all examples presented. Visual (VIS, 350nm-750nm) and near infrared (NIR, 1500nm-2000nm) luminosities are shown in (g); peak luminosities are indicated by vertical dashed lines. Image times corresponding to (a)-(f) are indicated on (g), and spectrometer exposure windows for each experiment are shaded in green. The collected spectra are shown in (h), where the spectral intensity I is normalized with respect to I*, the magnitude of the 396.1 nm Al I line of the Al/Al-90° configuration shown in Fig. 4. As such, all spectral intensities are plotted relative to the intensity of the dominant peak in the symmetric, Al/Al impact at normal incidence and the magnitudes of any spectral peak are read in comparison to that experiment. The first spectrometer exposure (#1) is measured with respect to the blue left-hand scale of (h); the second spectrometer exposure (#2)—which is generally much dimmer than the first and has been rescaled to visually match both 396.1 nm Al I peaks and make spectral shape differences easier to see—should be measured with respect to the red right-hand scale. For instance, in (h) it can be observed that the 396.1 nm Al I peak relative spectral intensity (I/I*) in the first exposure (#1) is 2.2 and the second exposure is (#2) 0.16. So the early exposure dominant Al emission peak for this experiment is over twice as intense as the Al/Al-90° impact, whereas the same peak has diminished in intensity by a factor of almost 14 by the late exposure.

spectra, as are Mg and Cu emissions (chief alloying elements in 6061Al). Fe and Cr species, from the 304SS projectile, can also be seen in spectrum #1, but are absent at the later time. The magnitude of all observable atomic peaks are reduced by at least an order of magnitude in the later-time spectrum. Significant Al-O molecular band emission[28] is present in spectrum #2, indicating the combustion of Al with ambient oxygen within the first 10 μs of the impact flash. While the overall intensity decays from #1 to #2 as indicated by the numerical peak magnitudes, the Al-O emission is the only component to increase relative to the atomic emission. The two spectra show that the significant combustion only occurs well after the luminosity peaks, demonstrating that combustion is not the chief cause of the light emitted during the times up to the peaks of the VIS and IR components of the flash. Thus the vaporized material is hot and radiating well before significant combustion occurs. Combustion emission was also observed at late times by Tandy et al[28] during the high velocity impact of nylon projectiles on aluminum plate in 1 Torr air. Oblique impacts for this projectile and target material combination and others are discussed in the Supplementary Information.

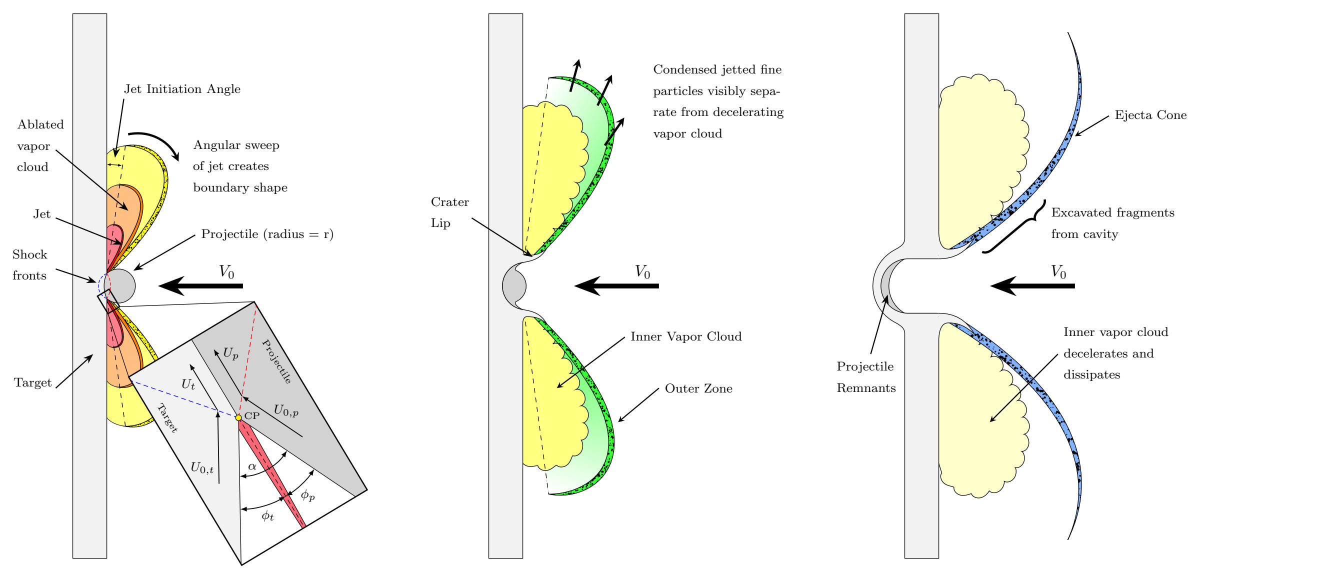

(a) Early Stage Jetting ($t \ll \tau$) (b) Transition Period ($t \approx \tau - 2\tau$) (c) Late Stage Excavation ($t \gg \tau$)

Figure 3: Cross sections of impact flash at early, transition, and late stages (not to scale). The initial stages of impact and flash formation by means of impact jetting are illustrated in (a). The characteristic time, $\tau = r_i/V_0$, represents the limiting timescale over which jet formation can occur. After initiation and during initial penetration, the impact jet sweeps out from the target creating an expanding annulus of radiating material. The collision point centered (CP) frame of reference used in jet initiation calculations is illustrated. The post-jetting ejection behavior begins to transition (b) to excavation of the impact crater. As the vapor cloud expands, cools, and decelerates relative to jetted particles, condensed phase material visibly separates from the vapor cloud. At later times, cavity excavation dominates the generation of fragments and the familiar ejecta cone develops fully (c). The target is nearly fully perforated as shown. The radiating vapor cloud dims and begins to dissipate.

Multiple mechanisms can contribute to an impact flash[13], but for these impact velocities we interpret our observations within the framework shown in Fig. 3. The impact event itself is divided into two primary stages: early-stage impact (during which the impact flash dominates observations) and late-stage impact and ejection (during which the impact crater develops and target perforation occurs). The representative timescale $\tau = r_i/V_0$ (where r_i is the projectile radius and V_0 the impact velocity) separates early-stage times from late-stage times. During first contact at these velocities, an impact jet forms due to the acute wedge angle (α) formed by the colliding surfaces of the target and impactor (Fig. 3a inset) [29]. This jet accelerates highly shocked and heated material outwards from the collision point of impactor and target. As the spherical projectile penetrates, the collision point and vertex of the wedge (wedge angle α) move outward, and the impact jet sweeps away from the target plane, such that material is jetted at steeper angles relative to the target surface. As the jet sweeps away from the target, the velocity of the jetted material also decreases[34]. The trajectories of jetted material and the nature of this sweep determines the morphology of the phenomena observed at early times. The jet may be intense enough to melt and vaporize material. Impact velocities much in excess of those investigated here are required to directly vaporize shocked material in the absence of a mechanism such as jetting. As the jetted material forming the flash expands, the apparent vapor cloud—which we attribute to the aerothermal ablation of small condensed particles, similar to that suggested by Sugita and Schultz[16] for polycarbonate projectiles impacting liquid targets—decelerates and dims. Radiating condensed-phase particles and fragments penetrate the boundary of the vapor cloud, creating the visual structure observed in Fig. 2d. As the projectile continues to penetrate the target, jetting terminates and a crater forms; the large scale ejection of solid fragments by the excavation of this crater forms the dark, visible front-surface ejecta cone traditionally associated with hypervelocity impact (Fig. 3b).

The operative mechanisms can be better understood by performing similar experiments using reciprocal and symmetric combinations of target and projectile materials, since the signatures of the mechanisms are strongly affected by the materials themselves. In addition to stainless steel impacting aluminum (SS/Al), we provide results for the symmetric case of Al impacting Al (Al/Al) and the reciprocal case of Al impacting SS (Al/SS), and, all at similar impact velocities. Obtaining the full set of diagnostics for each material pair allows identification and comparison of the key mechanisms in each case. We present the corresponding visualizations, photometry, and high-speed spectroscopy for these material pairs under normal incidence impact in Figs. 4 and 5. Relevant mechanical properties for all materials are presented in the supplementary information, together with results from additional configurations that clarify some nuances.

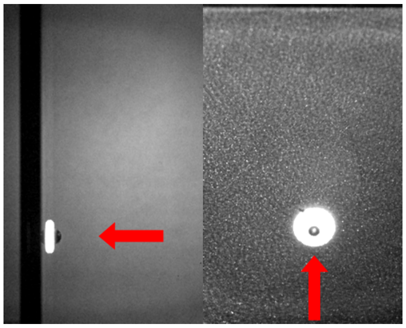

(a) $t = 0.2\ \mu s$

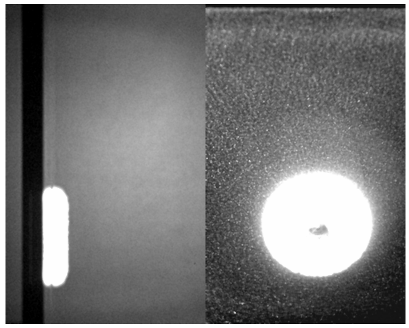

(b) $t = 1.2\ \mu s$

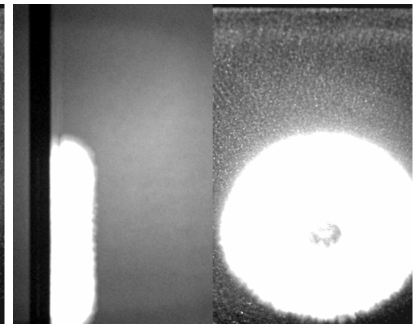

(c) $t = 2.8\ \mu s$

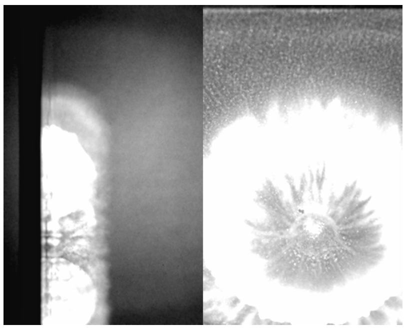

(d) $t = 4.6\ \mu s$

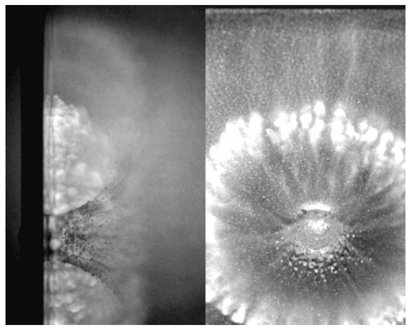

(e) $t = 7.4\ \mu s$

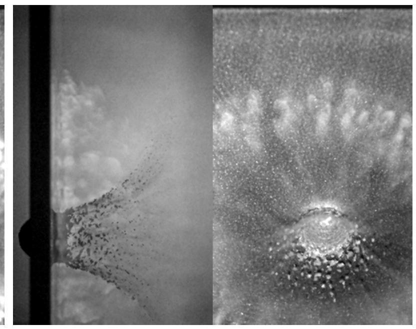

(f) $t = 10.6\ \mu s$

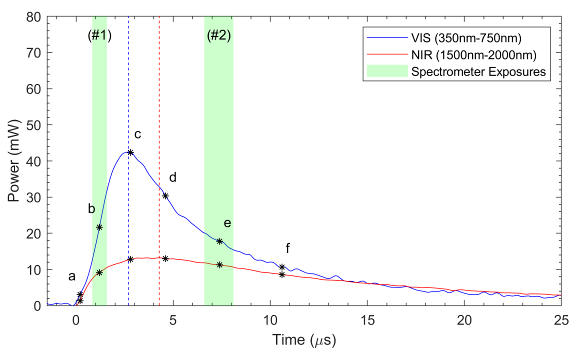

(g) Visual and Near-IR Luminosity

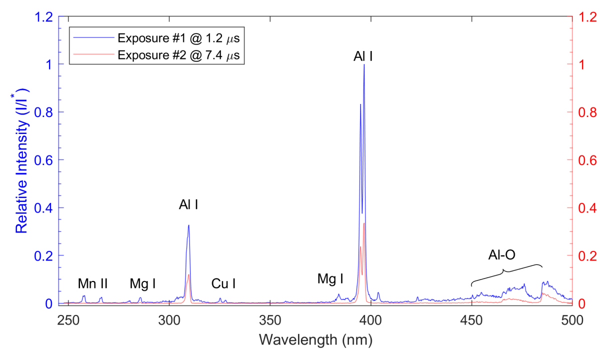

(h) UV-Visual Gated Spectra (250-500nm)

Figure 4: 2024Al projectile impacting 6061Al target at normal incidence with velocity of 3.2 km/s in 10 Torr air. See Fig. 2 for description of figure elements.

The symmetric materials case is shown in Fig. 4, with a 2024Al projectile impacting a 6061Al target at 3.2 $km\ s^{-1}$. The high-speed optical images (Fig. 4a-f) show that the impact flash develops by a similar process, with an outer component whose boundary transitions into the classical ejecta cone, and expands faster radially along the target plate. However, the outer component is less distinct in this case. The evolution of the luminosity (Fig. 4g) differs from that in Fig. 2g, with the maximum in the NIR luminosity now occurring *after* the maximum in the optical luminosity. While Al peaks still dominate the atomic emission, the molecular behavior differs greatly in that no significant increase in Al-O emission relative to the Al atomic peaks is observed. The spectral shapes of both early and late exposures are generally much more similar than was the case with the previous SS/Al impact shown in Figure 2, and the overall peak intensities do not decay as much. Neither Fig. 2g nor Fig. 4g show prompt emission—meaning narrow, fast-rising luminosity spikes produced immediately after impact. Prompt emission[10–12] indicates the presence of material vaporized *directly* by impact processes. The absence of such spikes within the first microsecond after impact would suggest no significant impact vaporization; however, the higher ambient pressure atmospheres used in this work (in excess of 1 Torr) may prevent clear observation of prompt emission spikes[11,13]. At the impact velocities investigated here, shock heating (maximized in the impact jet) is insufficient to vaporize these target and projectile materials, although it is sufficient to at least partially melt jetted material. Impact experiments on metals performed by Zhaoxia[11] under high vacuum, in which prompt spikes are observed above impact velocities above 5 $km\ s^{-1}$, also found no prompt emission at our impact velocities of 3 $km\ s^{-1}$. Our observed vapor phase characteristic emission is thus attributed to the ablation of fragments of condensed phase material that have broken off an impact jet.

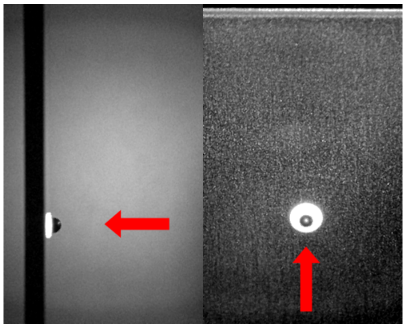

(a) $t = 0.2\ \mu s$

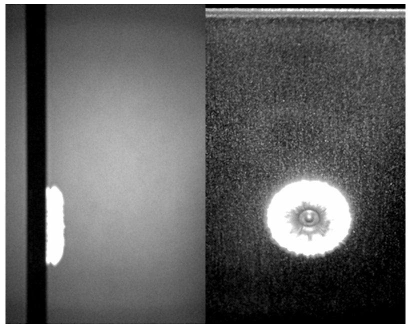

(b) $t = 1.0\ \mu s$

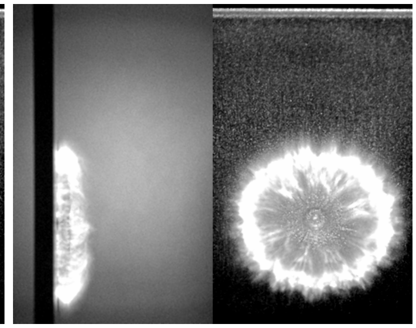

(c) $t = 2.6\ \mu s$

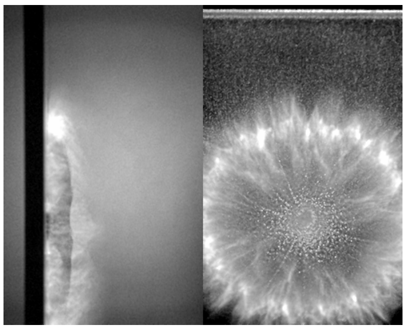

(d) $t = 4.6\ \mu s$

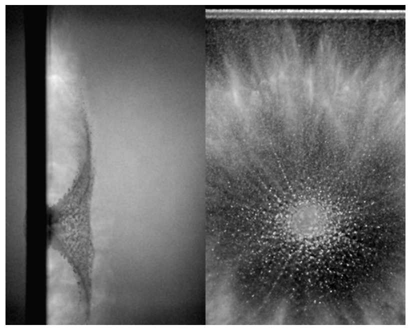

(e) $t = 8.0\ \mu s$

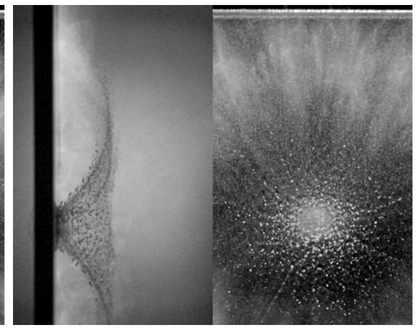

(f) $t = 10.6\ \mu s$

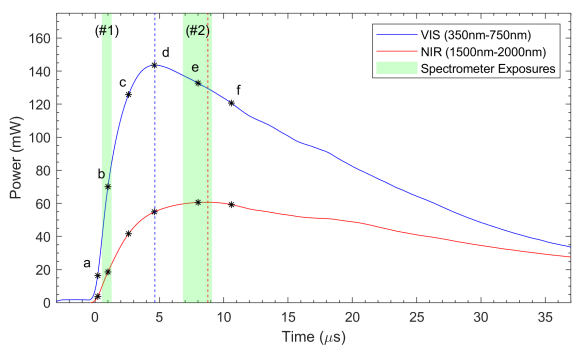

(g) Visual and Near-IR Luminosity

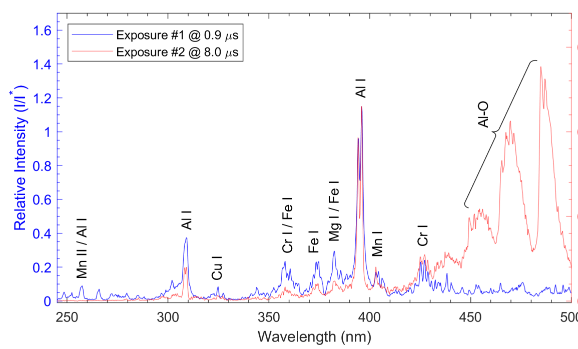

(h) UV-Visual Gated Spectra (250-500nm)

Figure 5: 2024-Al Projectile Impacting 304SS Target at 90°Obliquity with Velocity of 3.1 km/s in 15 Torr Air. See Fig. 2 for description of figure elements.

Qualitatively different phenomena are observed for the reciprocal materials arrangement, when a 2024Al sphere impacts a 304SS target plate at 3.1 kms^{-1} (Fig. 5). In this case the overall impact flash power was much higher, so that a 640nm CWL-40nm FWHM bandpass interference filter had to be used to allow proper visualization of the impact. As before, in Fig. 5a-c we see the initial radial and out-of-plane expansion of the bright emitting region. However, at later times, Fig. 5d-f, it is not clear that there is a separation between distinct inner and outer zones as brighter and darker emitting regions. The ejecta cone is also much shallower (Fig. 5e-f) than in previous configurations, and smaller ejecta particles are observed.

Fragmented particles are ejected from the developing crater as material flows radially out from the impact center and upwards from the target surface during target penetration. The flow of this material establishes the trajectories of late-stage ejecta fragments. Shallower craters provide shallower ejecta trajectories; as the crater deepens ejecta trajectories steepen relative to the target surface, usually approaching a steady, terminal value often referred to as the ejecta cone angle. In the case of the SS/Al and Al/Al impacts, steeply-walled deep transient craters form, leading to full perforation of the target. For Al impacting SS, there is insufficient impact energy to perforate this stronger target, leaving a shallow crater with correspondingly shallower wall angles at the target surface. Generally, lower density projectiles (e.g. polymer, aluminum) impacting denser targets (e.g. iron, steels, copper) will generate shallower craters with depth-to-diameter ratios of less than 0.4, whereas projectiles denser than their targets generate ratios of 0.6 or greater[35–38]. Increased relative target strength shows similar effects, generating shallower craters[39,40]. Terminal ejecta cone angles likewise become more shallow in these cases[41,42], as observed here.

Unlike the previous configurations, the continuity of ejecta cone and outer emission zone boundaries observed in Figs. 2 and 4 is not observed here, suggesting a change in the mechanisms. The outer flash boundary initially outruns the ejecta cone in Fig. 5c-d. Comparing Fig. 5g with Figs. 2g and 4g, we see that both the VIS and NIR peak luminosities far exceed those observed in the previous impacts (i.e., this configuration produces a much brighter flash). Comparing the spectra in Fig. 5h with those in Figs. 2h and 4h, we see that the Al-O emission dominates the observed spectrum in exposure #2 (note that additional molecular peaks in this series exist[28] beyond the 500nm range).

2.1 A Jet-based Mechanism for the Impact Flash

Impact jetting of condensed material that subsequently interacts with the atmosphere to generate the flash is the only mechanism consistent with all of these observations. The impact of a spherical projectile on a planar target provides an axisymmetric configuration with a monotonically increasing local wedge angle (α) between projectile and target surface, and the corresponding jetting theory is established[13,14,43,44]. The asymmetric jetting theory calculations performed here follow the methods described by Sugita and Schultz[14], Kurosawa[45], and Zhaoxia et al[13] as detailed in the supplementary material. The observed differences between Figs. 5 and 4 are a direct result of projectile and target material properties under these experimental conditions: classical asymmetric jetting theory predicts the initiation of the impact jet to occur in either the projectile or target depending upon shock properties and impact conditions. As such, we expect the flash behavior to be governed primarily by the hydrodynamic properties of the materials involved, while the main ejecta cone formation is sensitive to the strength properties and failure behavior of the materials.

At the moment jetting begins, the impact jet is an expanding conical sheet originating from the annular

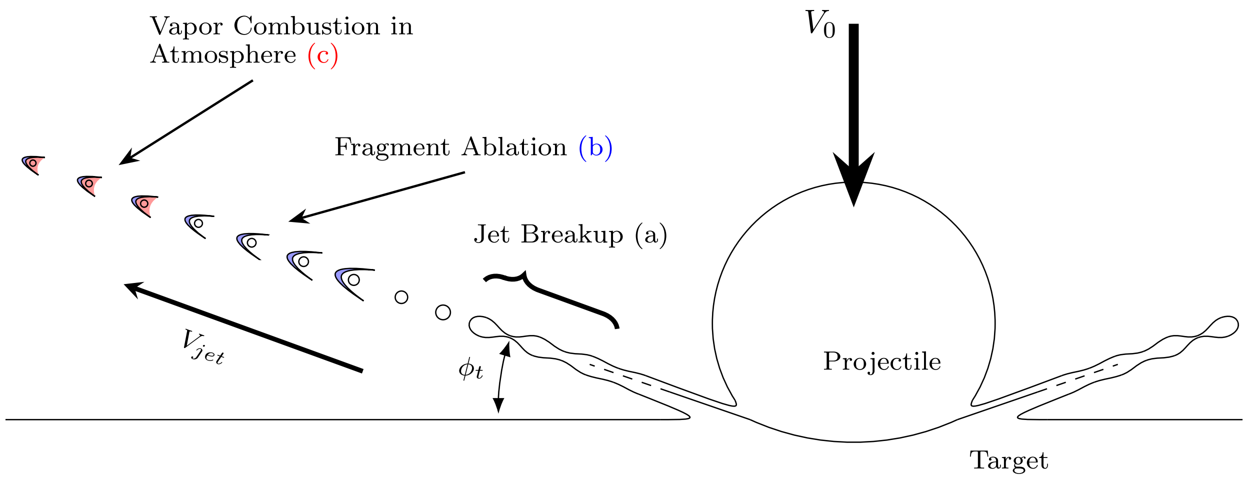

Figure 6: Lifetime of a jetted particle in the impact flash. The impact jet breaks up and fragments (a), as a result of its generally axisymmetric expansion and radial velocity gradient effectively stretching and thinning the jet sheet. The interaction of the expanding jet with the atmosphere may also contribute to the breakup. It is likely that the jet is at least partially molten, so the proper mechanical description of this breakup is somewhat nebulous. The generated fragments, having a a velocity V_{jet} and direction established by the deflection angle of the jet from the target plane, ϕ_t, begin to ablate and decelerate due to their high velocity (approx. Mach 30) movement through the rarefied ambient atmosphere (b). The ablated metallic vapor emits characteristically, producing identifiable atomic spectral peaks. As the ablated metallic vapor mixes with ambient oxygen, it combusts, producing the observed molecular Al-O emission. Note, the size of the jets and fragments in relation to the projectile are exaggerated here.

contact locus of the impactor as it penetrates the target surface. During these early times, with $t << \tau$, the jet angle steepens and sweeps outward from the target as penetration continues (see Fig. 3a). Newly jetted material moves along steeper trajectories than previously jetted material, with generally reduced velocities as the shock pressures decay. Investigations of planar shock-induced jetting at free metallic surfaces have shown the breakup of the jet sheet begins at the jet tip and propagates backwards towards the base of the jet[46]. We expect a similar breakup process to occur within a radially divergent metallic cone jet due to the development of instabilities[47], generating a size distribution of fragments[48]. The impact jet is at least partially molten at these impact velocities. The jet breaks up as it expands radially as shown in Fig. 6, with the jetted fragments experiencing the sequence of events described in the figure. Jet fragmentation begins at a critical stretch for a given stretching rate (and therefore at a critical time). The jetted fragments ablate and decelerate as they travel at very high velocities ($10\ km\ s^{-1}$) through the rarefied chamber atmosphere. The smaller fragments will then ablate and decelerate until they are consumed within a vapor cloud, while the larger fragments continue to travel at high velocity. Micron or submicron fragments ablate quickly, producing an intense cloud of radiating vapor. As this vapor cloud decelerates and mixes with the ambient atmosphere, it combusts with residual oxygen. The larger fragments experience continue to travel at high velocity with little ablation, and thus visibly separate from the vapor cloud. This process generates the two emission zones discussed previously.

To measure the deceleration of the outer emission boundary, the edge of the flash region was tracked along a radial trajectory at an inclination of 10° with respect to the target surface (this angle was chosen to correspond with the predicted critical jet initiation angle relative to the target surface). The motion of the outer emission boundary was fit with a thermally ablative drag model[49], previously applied to impact flash[13] but classically used for the analysis of meteor ablation. The results of the ablation model are presented in Fig. 7a, with details in the supplementary material. Simulations[46,50] and experimental measurements[51] of planar shock induced sheet jet breakup have suggested exponential distributions in fragment volume (such exponential distributions in fragment volume/mass are commonly applied to fragmentation problems[48]). The model fit suggests a mean initial particle diameter of approximately 3.3 μm for the ablating (smaller) particles in the fragment size distribution.

We can estimate the shape of the luminosity curve from the flash as a consequence of this jet-based mechanism. A thermally ablative drag model[11,49] for spherical particles (see Supplementary Information) estimates the luminosity generated by a particle size and velocity distribution in a prescribed ambient atmosphere. This primary input is modified because at early times some jetted particles block other radiating particles from sensor view, diminishing the observable luminosity of the flash cloud and providing a "rise time" in the luminosity (the self-occlusion formulation is in the supplementary information). Particle self-occlusion effectively controls the rise behavior of the observed luminosity, and the peak luminosity is determined by the competition of the total decaying ablation luminosity of the particle cloud and the increasing visibility of that luminosity as self-occlusion decreases. The apparent rise time of flash luminosity, at least in atmospheres dense enough to provide rapid ablation of fragments, is a consequence of the interaction of these generative and occlusive terms.

The experimentally observed luminosity of an Al/Al impact was fit assuming the thermally ablative radiation of an exponential distribution of spherical particles, accounting for self-occlusion. The resulting average particle diameter and model luminosity curve is shown in Fig. 7c. This luminosity fit suggests a mean initial fragment diameter of 2.3 μm. The corresponding particle distribution is shown in Fig. 7d, where the particle volume follows an exponential distribution. The 3.3 μm size estimated through fitting the boundary position (Fig. 7a) would represent the 95th percentile fragment size in this distribution. It is reasonable to expect the fit to the emission zone boundary motion to reflect a fraction of larger size particles that maintain their velocity, and in this light the comparison between the ablating particle size estimate from the luminosity calculation and the particle size estimate from the emission zone boundary measurement is very good. This supports our postulated mechanism of a jet-induced particle ablation origin for the impact flash in our experiments.

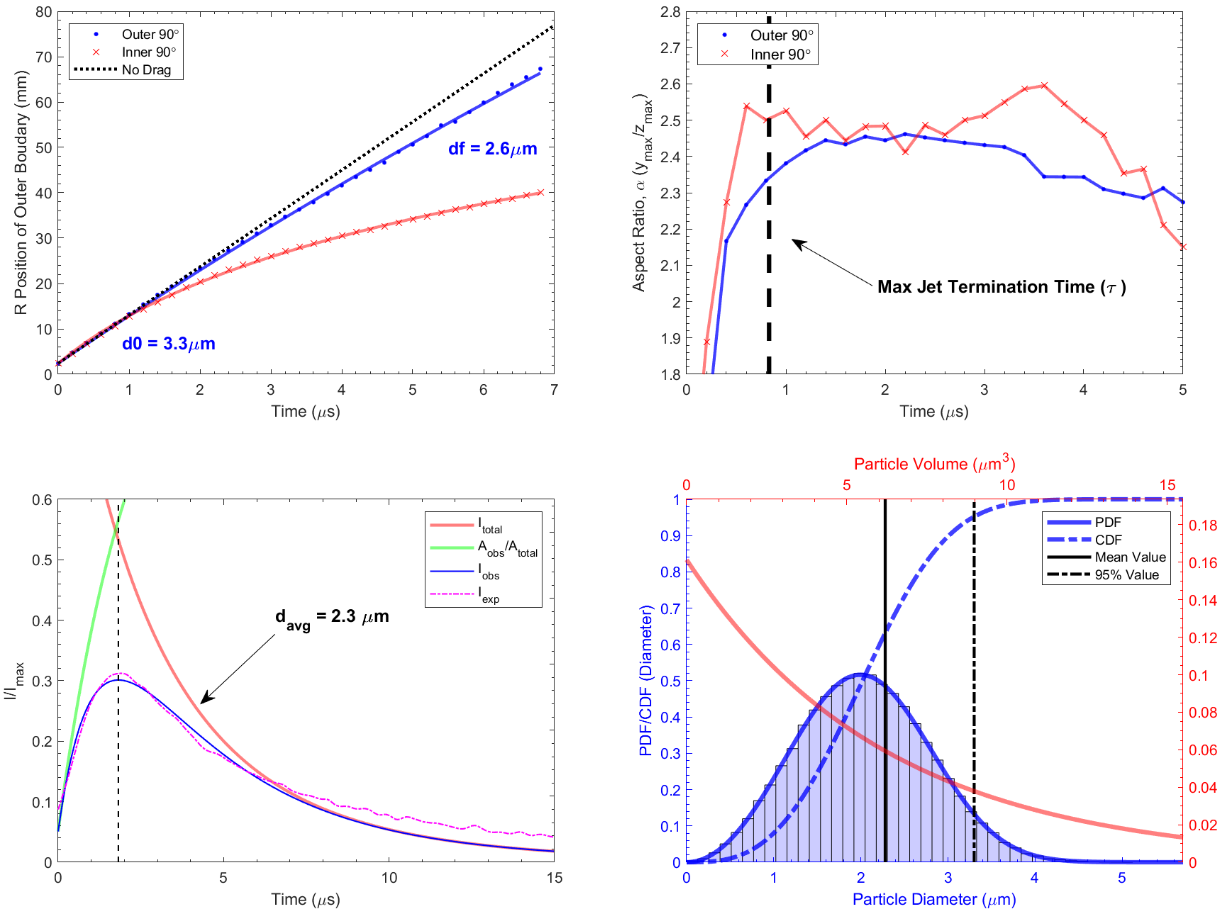

Figure 7: Al/Al flash expansion and luminosity analysis assuming particle cloud ablation. Experimental data presented for Al/Al impact at 3 km/s in 11 Torr air. The position of the outer emission front along the 10° radial from the target plane (a) was fit using a thermally ablative aerodynamic drag model assuming single sized spherical molten aluminum particles constituting the boundary of the flash. The aspect ratio of the flash given by the maximum (+y direction) height and (+z direction) width of the imaged cloud is given in (b), and generally plateaus within τ, the maximum approximate limiting time over which jetting can occur. The observed variations in aspect ratio at times over 3 μs is due to degrading boundary definition in the experimental images as the flash intensity begins to decay.The calculated observable ablation luminosity (I_{occ}) of an expanding spherical shell particle cloud is given in (c), assuming partial self-occlusion ratio A_{obs}/A_{total}. The calculated theoretical ablation intensity of the particle cloud is maximized here at $t = 0$, where the initial velocity of each particle is highest. Zero time is shifted by $\tau = r_i/V_0$ to account for the formation time of the jetted particle cloud. Self-occlusion at early times diminishes the observable luminosity, and is assumed here to vary as the ratio of observable particle surface area (A_{obs}) to total particle area (A_{total}). The observable luminosity is fit to experimental data to determine an initial average fragment diameter. The particle distribution shape is assumed to be exponential in volume. The volume (red) and size (blue) distributions (PDF) determined by the model fit shown in (c) are given in (d). The CDF of fragment size is also shown.

The shape of the model luminosity curve does not fully reproduce the decay of the experimental curve; a better description of the radiation physics involved is almost certainly necessary to improve this fit. The classical thermal meteor ablation model used here does not account for alternative erosive mechanisms that may be at play in the largely molten fragments or for the evolution of the radiating vapor, for example. One potential source of energy that may affect the later decay of overall observed VIS luminosity is the reaction of ablated vapor with atmospheric oxygen; oxide emission in the VIS range tends to dominate the emitted spectra at later times.

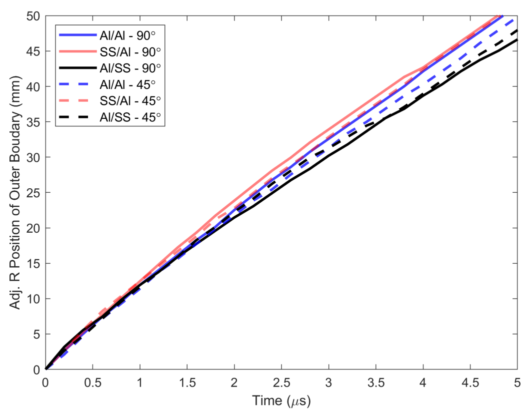

(a) Emission Front Positions Along 10° Radial

(b) Maximum Emission Front and Predicted Jet Velocities for All Configurations

	Al/Al		SS/Al		Al/SS	
	90°	45°	90°	45°	90°	45°
P_{atmo} (Torr)	9.8	15.0	15.2	15.0	15.0	15.3
V_{impact} (km/s)	3.21	3.11	3.02	3.03	3.07	3.03
$P_{jet,max}$ (GPa)	57.1	38.7	70.6	61.5	73.9	51.1
$V_{jet,exp}$ (km/s)	11.6	11.4	12.3	12.0	11.3	11.5
$V_{jet,\,theor}$ (km/s)	19.9	20.5	21.2	19.1	20.7	22.0
f_{exp}	0.17	0.09	0.16	0.21	0.10	≈ 0

Figure 8: Measured emission front position and jet velocities (km/s) for All Experiments. The experimental jet velocities ($V_{jet,exp}$) given in (b) are measured by fitting the ablative drag model to the data in (a). The maximum hydrodynamic shock pressure achieved in the jet ($P_{jet,max}$) and the ideal jet velocity ($V_{jet,ideal}$) are calculated assuming critical initiation conditions.

Note that the calculation of lab frame jet velocity in standard jetting theory uses a parameter f[29] that relates the jet velocity to the effective flow velocity of material into the collision point (indicated by point CP in Fig. 3a). Foundational work on jetting showed that $f \approx 1$ for colliding thin plates.[29,30]. Kurosawa's experiments showed that such a theory overpredicted measured jet velocities by approximately 30%[45] using polycarbonate projectiles with similar impact geometry and velocities to this work. They found $f \approx 0.4-0.8$ depending upon impact conditions and materials. This discrepancy can be explained in part by the decay of shock pressure during spherical jetting as the newly initiated jet envelops and expels mass. It takes some time after initiation for substantial mass to be engulfed into the jet, and by this time the driving pressure associated with the jet may have decayed[34,52]. Here, we calculate an experimental value of f similarly to Kurosawa et al[45] (see supplementary material equation (5)). The resulting experimentally determined f values, ideal jet velocities, relevant experimental conditions, and experimental jet velocities (measured by ablative drag fit of the outer flash boundary) for all configurations tested are shown in Fig. 8. The standard theory ($f = 1$ at critical initiation) overpredicts the jet velocities by $60-90\%$. Our experimentally estimated f values are much lower than those measured by Kurosawa. This large discrepancy may reflect our modeling approximations.

2.2 Jet Initiation and the Distinctive Behavior of Al on SS Impacts

Our impacts are fundamentally asymmetric even if the materials are the same because the projectile is spherical and the target planar. Thus one side of the impact will reach criticality—when the deflection angle, ϕ, associated with the oblique shock in either target or projectile exceeds the critical angle, ϕ_{cr}, as indicated in Fig. 3a—initiating the jet in the critical material (see supplementary material). While it is expected and observed that material on the non-initiating side is quickly entrained into the jet, the predicted initiation of the jet still provides insight into the nature of early-time material ejection during an impact. Our predicted jet initiations for the SS/Al and Al/SS impact configurations are shown in Fig. 9. The jet is predicted to initiate in the target material for the SS/Al configurations, but in the projectile material for the Al/SS configurations. Indeed, the materials used here have sufficiently different wave speeds that the Al structure will see critical deflection first in all cases. This gives us insight into why there is a change in flash/ejecta boundary continuity when the projectile and target materials are swapped.

When SS impacts Al, the jet is predicted to initiate in the target (Fig. 9a-b). Note that the jet evolution and associated flash behavior also depend upon the hydrodynamic properties of the non-initiating side (the projectile in this case). As the jet terminates, the material ejection mechanism transitions to excavation of the impact crater. The excavation process under these impact conditions depends upon the interaction of both projectile and target during penetration, but the trajectories of excavated ejecta are strongly linked to the evolution of the crater geometry (controlled by the target material response). In this configuration, the ejected fragment trajectories are primarily controlled by the target side material at both stages and the transition from early-time jetting to late-time excavation involves processes dominated by the same material characteristics, that of the target. This smooth mechanistic transition provides a continuous set of fragment trajectories as jetting subsides and crater ejection begins. This manifests in the observed continuous transition of flash boundary to ejecta cone boundary in SS/Al impacts.

In the case of both normal and oblique Al on SS impacts, the jet is predicted to initiate on the projectile side (Fig. 9c-d), as opposed to the target side. As such, the material side controlling the trajectories of ejected fragments may effectively switch from projectile to target as early-stage jetting transitions to later-stage crater excavation. This jump from projectile controlled ejection to target controlled ejection

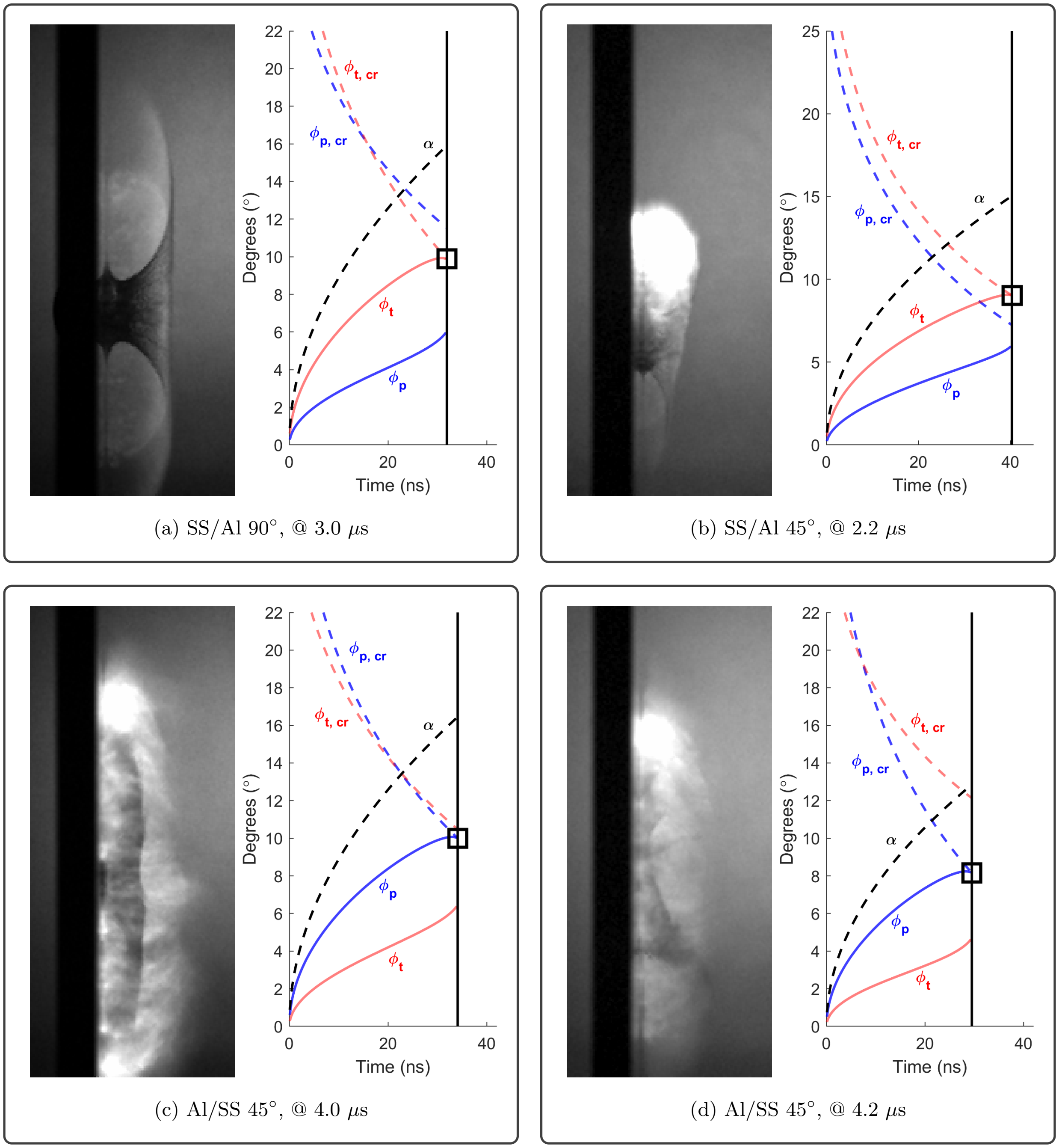

(a) SS/Al 90°, @ 3.0 μs

(b) SS/Al 45°, @ 2.2 μs

(c) Al/SS 45°, @ 4.0 μs

(d) Al/SS 45°, @ 4.2 μs

Figure 9: Flash/ejecta behavior and predicted jet initiation. Selected narrow-band filtered images from the SS/Al and Al/SS impacts are shown. The typical experimental result for (b) is given in Supplementary material. The deflection angle of the material flow in the collisional frame is given by ϕ. Jet initiation is predicted when ϕ reaches its respective critical value, ϕ_{cr}, such that $\phi_{cr} - \phi = 0$. The initiation conditions are boxed in the figure. In the case of the SS/Al configurations, jet initiation is predicted to occur in the target (a),(b). However, jet initiation is predicted to occur in the projectile for the Al/SS configurations (c),(d). The wedge angle between projectile and target surfaces is given by α, and the initiation time is marked by the vertical line.

results in the observed lack of continuity between the flash and ejecta cone boundaries when Al impacts SS. In contrast to the previous case, jetting and excavation must be considered as distinct and separate mechanisms controlled by different material properties (the projectile during jetting and mostly the target during excavation). Note, eroded projectile material comprises much of the solid excavated ejecta in the Al/SS configuration, as the crater development and size is limited, but the crater geometry and shape are largely governed by the steel target material properties and therefore the character of the excavation process is still heavily target dependent. However, more work is needed to understand and quantify these mechanisms.

The contrast between continuous and discontinuous jet and ejection behavior could provide a strong signature for future models capable of capturing both multi-phase impact jetting and crater growth phenomena. The traditional limitations of the hydrocodes often used to model shock physics and Lagrangian finite element methods commonly used to model solid mechanics phenomena have usually required researchers to target specific mechanisms, and even cutting edge modeling methods are challenged by multiple physical states and mechanisms. However, to advance physical understanding of such complex coupled phenomena as the effects of impact-generated ablative fragment clouds on the aerodynamics of surfaces and hypersonic boundary flows, more detailed experiments addressing mechanisms across the full range of the problem will be required. Future multiphysics modeling approaches will need a variety of empirical signatures for validation, and phenomena similar to those observed in these experiments may provide just those valuable signatures.

3 Conclusions

Previous hypervelocity impact studies have separately investigated the phenomena of impact flash and the mechanics of material ejection in various impact configurations. The experiments performed here interrogate both flash and ejecta in one system by using in situ time-resolved diagnostics, and we have observed several interesting connections between these two phenomena in metals. Our experiments demonstrate a mechanistic connection between radiating flash phenomena and ejecta cone formation. We show that under these impact conditions the impact flash is driven by ablation of particles fragmented from the impact jet, and we are able to obtain estimates of jetted particle size based upon observations of the impact flash evolution alone. These approaches provide a way to interrogate highly dynamic condensed matter jetting phenomena at larger spatio-temporal scales.

4 Experimental Methods

4.1 Impact Configurations

All of the experiments were performed at the Hopkins Extreme Material Institute HyFIRE (Hypervelocity Facility for Impact Research Experiments) facility. The facility was designed to provide experimental versatility over a variety of high velocity and hypervelocity impact conditions, and provides flexible *in situ* time-resolved diagnostics[53] with an emphasis on quantification and visualization. The core launch capability in HyFIRE is a small-bore (7.62 mm) two-stage light gas gun that provides launch velocities exceeding 5 $km\ s^{-1}$ for 1 g launch packages. Our experiments studied the mechanisms developed during the high-velocity impact (at 3 $km\ s^{-1}$) of 5 mm spheres onto 6.35 mm thick target plates at normal incidence (90°) and 45° impact obliquity. The impactors were made of either 2024 aluminum alloy (2024 Al) or 304 stainless steel (304SS), while the target plates were made of either 6061-T6 aluminum (6061Al) or 304SS. Thus the projectile/target material combinations were 2024Al/6061Al (Al/Al), 304SS/6061Al (SS/Al), and 2024Al/304SS (Al/SS). All of the impacts occurred in air within a target chamber evacuated to approximately 10-15 Torr. The target and diagnostic configurations are shown in Fig. 10; the diagnostics used consisted of optical ultra-high-speed video, emission spectroscopy, and broadband luminosity monitoring.

4.2 Optical Imaging

Optical ultra-high-speed video was configured to observe both the optically radiating material contributing to the early impact flash (referred to here as "hot" ejected material) and the solid material and fragments forming the traditional late-stage ejecta cone (referred to as "cold" ejected material). Two Shimadzu HPV-X2 cameras were used to view the impact, one oriented to view the impact perpendicular to the shot axis (Side View in Fig. 10) with the target in profile, and the second oriented to view the target front (impacted) surface from an angle 30° from the shot axis (Front View in Fig. 10, and thus orthogonal to the lens axis of the first camera). Illumination was provided by a synchronized Cavitar illumination laser providing reflected illumination for the front camera, and diffused monochromatic backlighting for the side view camera[54]. All data presented was captured at 5 Mfps with approximately 110ns exposures. The backlight illumination was configured to provide center region mid-level grayscale, darkening towards the periphery of the frame, so that hot expanding material and cold center ejecta could be tracked with high contrast in any single experiment. Monochromatic illumination was used to facilitate partial bandpass filtering of the flash when desired, without affecting the cold material contrast; this also allowed simultaneous emission spectroscopy and impact flash monitoring without interference from broadband illumination sources. For all Al/SS impacts,

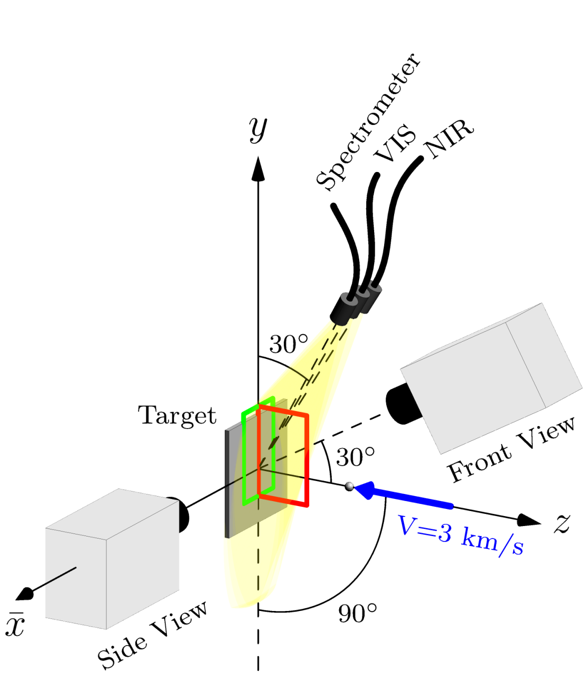

(a) Normal Incidence (90°) Configuration

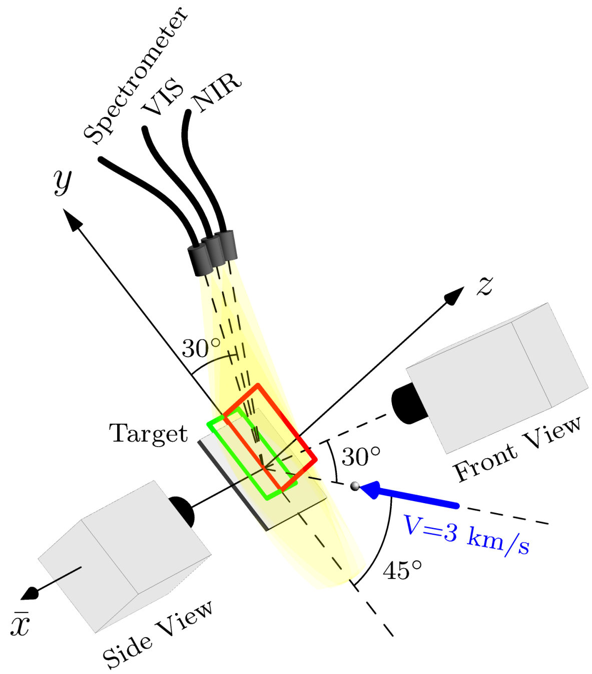

(b) 45° Oblique Configuration

Figure 10: Impact and diagnostic configurations. Both the side view camera field-of-view (red) and front camera field-of-view (green) are approximately 65mm (W) x 105mm (H).The side view camera is rotated with the target for oblique impacts, such that the coordinate axes are maintained with respect to the target surface.The front view is fixes with respect to the projectile velocity vector. Spectrometer, VIS, and, NIR luminosity collection optics are oriented at 30° to the target plane, collecting roughly an 8" diameter field-of-view at the target and fiber coupled to the UV/VIS spectrometer and photodiodes, respectively. The collection optics view the impact from the top of the impact chamber to reduce coupling of camera illumination to the VIS detector and are rotated with the target to maintain relative orientation to the target surface under oblique impact.

the high impact flash intensity demanded the use of 650nm CWL imaging intereference filters with 40nm FWHM passbands to partially suppress flash intensity.

4.3 Emission Spectroscopy and Flash Intensity Monitoring

Optical impact flash emission spectra were collected using a Princeton Instruments SCT-320 imaging spectrometer coupled to a PIMAX4 1024i (200-900nm spectral range, with 1024x1024 pixel detector) interline ICCD camera that allows the collection of multiple gated, intensified exposures over the duration of a typical event. Two UV/VIS spectrometer exposures were taken during each impact experiment; the first exposure triggered as soon as possible after impact (typically centered about 1 μs after impact), and the second exposure was centered approximately 8 μs after impact. The duration of and specific timing of each exposure is noted in the results section, but the first exposure was typically 750ns long (occurring before peak flash visual intensity) and the second exposure was typically three times as long to help balance signal intensity with the brighter early exposure. The spectrometer collection itself was triggered by the rising signal from an amplified Si photodiode (VIS detector in Fig. 10) collecting visual emission from the impact site. An amplified InGAs photodiode collected near-infrared emission (NIR detector) with similar optics and viewing as accompanied the visual detector. The photodiode optics were filtered such that the VIS detector covered a spectral range from 300 $nm - 750$ nm, while the NIR detector covered 1500 $nm - 2000$ nm. A similarly mounted, polarization-resistant fiber-coupled UV fused silica optic with approximately the same FOV as the photodiodes provided UV/VIS emission to the spectrometer. The emission spectrum from approximately 250 $nm - 500$ nm is analyzed in the present work, requiring the use of UV silica window insets on the top chamber bulkhead to transmit the required wavelengths. The resulting configuration provided in situ time-resolved luminous intensity measurements over the 300 $nm - 750$ nm VIS and 1500 $nm - 2000$ nm NIR bands, as well as gated emission spectra from 250 $nm - 500$ nm collected from the same FOV and viewing angle.

References

1. Karako, T. & Dahlgren, M. Complex Air Defense: Countering the Hypersonic Missile Threat. *A Report of the CSIS Missile Defence Project, Center for Strategic & International Studies. https://www. csis. org/analysis/complex-air-defence-countering-hypersonic-missile-threat* (2022).
2. `https://airandspace.si.edu/multimedia-gallery/100520-f-9999b-111jpg`.
3. `https://cdn.mos.cms.futurecdn.net/q6L8JJJgz7TdtQEgYywEYU-1200-80.jpg`.
4. `https://blogs.nasa.gov/spacestation/wp-content/uploads/sites/240/2021/12/blog\_jsc2021e064216\_alt.jpg`.
5. `https://www.nasa.gov/sites/default/files/thumbnails/image/16658886757\_69219ed7f8\_k.jpg`.
6. `https://ualr.edu/geology/files/2006/10/EarthHorizon.png`.
7. Gehring, J. & Warnica, R. Investigation of the reaction of the lunar surface to the impact of a lunar probe final report (1963).
8. Eichhorn, G. Measurements of the light flash produced by high velocity particle impact. *Planetary and Space Science* **23,** 1519–1525 (1975).
9. Eichhorn, G. Primary velocity dependence of impact ejecta parameters. *Planetary and Space Science* **26,** 469–471 (1978).

10. Jean, B & Rollins, T. Radiation from hypervelocity impact generated plasma. *Aiaa Journal* **8,** 1742–1748 (1970).

11. Zhaoxia, M., Anhua, S., Junling, L., Pei, L. & Sen, L. Radiation evolution characteristics of the ejecta cloud produced by aluminum projectiles hypervelocity impacting aluminum plates. *International Journal of Impact Engineering* **138,** 103480 (2020).

12. Yanagisawa, M, Kurosawa, K & Hasegawa, S. Ultra-High-Speed Photography and Optical Flash Measurement of Nylon Sphere Impact Phenomena. *Procedia Engineering* **103,** 657–662 (2015).

13. Zhaoxia, M. *et al.* Radiation mechanism analysis of hypervelocity impact Ejecta cloud. *International Journal of Impact Engineering* **141,** 103560 (2020).

14. Sugita, S. & Schultz, P. H. Spectroscopic characterization of hypervelocity jetting: Comparison with a standard theory. *Journal of Geophysical Research: Planets* **104,** 30825–30845 (1999).

15. Ang, J. A. Impact flash jet initiation phenomenology. *International Journal of Impact Engineering* **10,** 23–33 (1990).

16. Sugita, S. & Schultz, P. H. Interactions between impact-induced vapor clouds and the ambient atmosphere: 2. Theoretical modeling. *Journal of Geophysical Research: Planets* **108** (2003).

17. Swaminathan, P., Brown, R. & Ramesh, K. *Predicting Optical Signatures from a Simple Impact Experiments* 2010.

18. Sugita, S. & Schultz, P. H. Interactions between impact-induced vapor clouds and the ambient atmosphere: 1. Spectroscopic observations using diatomic molecular emission. *Journal of Geophysical Research: Planets* **108** (2003).

19. Sugita, S., Schultz, P. H. & Adams, M. A. Spectroscopic measurements of vapor clouds due to oblique impacts. *Journal of Geophysical Research: Planets* **103,** 19427–19441 (1998).

20. Schultz, P., Sugita, S, Eberhardy, C. & Ernst, C. The role of ricochet impacts on impact vaporization. *International journal of impact engineering* **33,** 771–780 (2006).

21. Schultz, P. H. & Eberhardy, C. A. Spectral probing of impact-generated vapor in laboratory experiments. *Icarus* **248,** 448–462 (2015).

22. Goel, A, Lee, N & Close, S. Estimation of hypervelocity impact parameters from measurements of optical flash. *International Journal of Impact Engineering* **84,** 54–63 (2015).

23. Hew, Y. M., Goel, A, Close, S & Lee, N. Hypervelocity impact flash and plasma on electrically biased spacecraft surfaces. *International Journal of Impact Engineering* **121,** 1–11 (2018).

24. Kadono, T. & Fujiwara, A. Observation of expanding vapor cloud generated by hypervelocity impact. *Journal of Geophysical Research: Planets* **101,** 26097–26109 (1996).

25. Fuse, R., Abe, S., Yanagisawa, M. & Hasegawa, S. An experimental study of the impact flash: The relationship between luminous efficiency and vacuum level. *Planetary and Space Science* **187,** 104921 (2020).

26. Yafei, H. *et al.* Evolutionary characteristics of thermal radiation induced by 2A12 aluminum plate under hypervelocity impact loading. *International Journal of Impact Engineering* **125,** 173–179 (2019).

27. Mihaly, J., Tandy, J., Adams, M. & Rosakis, A. In situ diagnostics for a small-bore hypervelocity impact facility. *International Journal of Impact Engineering* **62,** 13–26 (2013).

28. Tandy, J. D., Mihaly, J. M., Adams, M. & Rosakis, A. Examining the temporal evolution of hypervelocity impact phenomena via high-speed imaging and ultraviolet-visible emission spectroscopy. *Journal of Applied Physics* **116,** 034901 (2014).

29. Walsh, J., Shreffler, R. & Willig, F. Limiting conditions for jet formation in high velocity collisions. *Journal of Applied Physics* **24,** 349–359 (1953).

30. Harlow, F. H. & Pracht, W. E. Formation and penetration of high-speed collapse jets. *The Physics of Fluids* **9,** 1951–1959 (1966).

31. Kieffer, S. *Impact conditions required for formation of melt by jetting in silicates* in *Impact and Explosion Cratering: Planetary and Terrestrial Implications* (1977), 751–769.

32. Frost, D. L., Zarei, Z. & Zhang, F. Instability of combustion products interface from detonation of heterogeneous explosives (2005).

33. Kramida, A., Yu. Ralchenko, Reader, J. & and NIST ASD Team. NIST Atomic Spectra Database (ver. 5.9), [Online]. Available: `https://physics.nist.gov/asd` [2017, April 9]. National Institute of Standards and Technology, Gaithersburg, MD. 2021.

34. Johnson, B., Bowling, T. & Melosh, H. Jetting during vertical impacts of spherical projectiles. *Icarus* **238,** 13–22 (2014).

35. Murr, L. *et al.* The low-velocity-to-hypervelocity penetration transition for impact craters in metal targets. *Materials Science and Engineering: A* **256,** 166–182 (1998).

36. Hernandez, V. S., Murr, L. E. & Anchondo, I. Experimental observations and computer simulations for metallic projectile fragmentation and impact crater development in thick metal targets. *International Journal of Impact Engineering* **32,** 1981–1999 (2006).

37. Valerio-Flores, O., Murr, L. E., Hernandez, V. & Quinones, S. A. Observations and simulations of the low velocity-to-hypervelocity impact crater transition for a range of penetrator densities into thick aluminum targets. *Journal of materials science* **39,** 6271–6289 (2004).

38. Marchi, S *et al.* Hypervelocity impact experiments in iron-nickel ingots and iron meteorites: Implications for the NASA Psyche mission. *Journal of Geophysical Research: Planets* **125,** e2019JE005927 (2020).

39. Ferreyra, E. T., Murr, L., Garcia, E. & Horz, F. Effect of initial microstructure on high velocity and hypervelocity impact cratering and crater-related microstructures in thick copper targets: Part I Soda-lime glass projectiles. *Journal of materials science* **32,** 2573–2585 (1997).

40. Murr, L. *et al.* Effect of initial microstructure on high velocity and hypervelocity impact cratering and crater-related microstructures in thick copper targets: Part II Stainless steel projectiles. *Journal of materials science* **32,** 3143–3156 (1997).

41. Nishida, M., Hiraiwa, Y., Hayashi, K. & Hasegawa, S. Ejecta cone angle and ejecta size following a non-perforating hypervelocity impact. *Procedia Engineering* **103,** 444–449 (2015).

42. Nishida, M., Kuzuya, K., Hayashi, K. & Hasegawa, S. Effects of alloy type and heat treatment on ejecta and crater sizes in aluminum alloys subjected to hypervelocity impacts. *International Journal of Impact Engineering* **54,** 161–176 (2013).

43. Vickery, A. M. The theory of jetting: Application to the origin of tektites. *Icarus* **105,** 441–453 (1993).

44. Miller, G. H. Jetting in oblique, asymmetric impacts. *Icarus* **134,** 163–175 (1998).

45. Kurosawa, K. *et al.* Dynamics of hypervelocity jetting during oblique impacts of spherical projectiles investigated via ultrafast imaging. *Journal of Geophysical Research: Planets* **120,** 1237–1251 (2015).

46. Durand, O. & Soulard, L. Modeling from molecular dynamics simulations of ejecta production induced by shock-loaded metallic surfaces. *Journal of Dynamic Behavior of Materials* **3,** 280–290 (2017).

47. Xavier, M *et al.* Extension of linear stability analysis for the dynamic stretching of plates: Spatio-temporal evolution of the perturbation. *European Journal of Mechanics-A/Solids* **79,** 103860 (2020).

48. Grady, D. *Fragmentation of rings and shells: the legacy of NF Mott* (Springer Science & Business Media, 2007).

49. Bronshten, V. A. *Physics of meteoric phenomena* (Springer Science & Business Media, 2012).

50. Durand, O & Soulard, L. Power law and exponential ejecta size distributions from the dynamic fragmentation of shock-loaded Cu and Sn metals under melt conditions. *Journal of Applied Physics* **114,** 194902 (2013).

51. Sorenson, D. S. *et al. Ejecta particle-size measurements in vacuum and helium gas using ultraviolet in-line Fraunhofer holography* tech. rep. (National Security Technologies, LLC.(NSTec), Los Alamos, NM (United States), 2014).

52. Wakita, S., Johnson, B. C., Denton, C. A. & Davison, T. M. Jetting during oblique impacts of spherical impactors. *Icarus* **360,** 114365 (2021).

53. Simpson, G., Shaeffer, M. & Ramesh, K. HyFIRE: Hypervelocity Facility for Impact Research at Johns Hopkins University. *Bulletin of the American Physical Society* **64** (2019).

54. Mallick, D. *et al.* Laser-driven flyers and nanosecond-resolved velocimetry for spall studies in thin metal foils. *Experimental Mechanics* **59,** 611–628 (2019).

55. Data, L. S. H. & Marsh, S. *Los Alamos Series on Dynamic Material Properties* 1980.

56. *Online materials information resource* `https://www.matweb.com/`.

57. Black, T. J. & Cheviakov, A. F. 3DRSP: Matlab-based random sphere packing code in three dimensions. *SoftwareX* **18,** 101051 (2022).

58. Grady, D. *Physics of Shock and Impact, Volume 2* (IOP Publishing, 2017).

59. Johnson, B. C., Minton, D. A., Melosh, H. & Zuber, M. T. Impact jetting as the origin of chondrules. *Nature* **517,** 339–341 (2015).

Acknowledgements

The authors were supported in part by the Defense Threat Reduction Agency (HDTRA1-18-1-0016) and U.S. Army Research Laboratory through the Materials in Extreme Dynamic Environments CRA (Cooperative Agreement Number W911NF-12-2-0022). The authors would like to acknowledge the Hopkins Extreme Materials Institute (HEMI), Army Research Laboratory, and the Johns Hopkins University Applied Physics Laboratory for supporting the establishment and the ongoing development of the HyFIRE facility. The views and conclusions contained in this document are those of the authors and should not be interpreted as representing the official policies, either expressed or implied, of the Army Research Laboratory or the U.S. Government. The U.S. Government is authorized to reproduce and distribute reprints for government purposes notwithstanding any copyright notation herein. Finally the authors would like to thank current and former members of the Ramesh, Foster, and Weihs research groups at JHU, including Debjoy Mallick, Yunho Kim, Pinkesh Malhotra, Jesse Grant, Roberto Nunez, and Milad Alemohammad.

Author Contributions

Gary Simpson: conceptualization and design of methodology, data acquisition and analysis, writing-original draft, review and editing. Matt Shaeffer: data acquisition and facility development. Justin Moreno: data acquisition and facility development. K.T. Ramesh: conceptualization and design of methodology, research supervision, acquisition of resources and funding, writing-original draft, review and editing.

Competing Interests

The authors declare no competing interests.

Supplementary Material

Jet Initiation Calculations

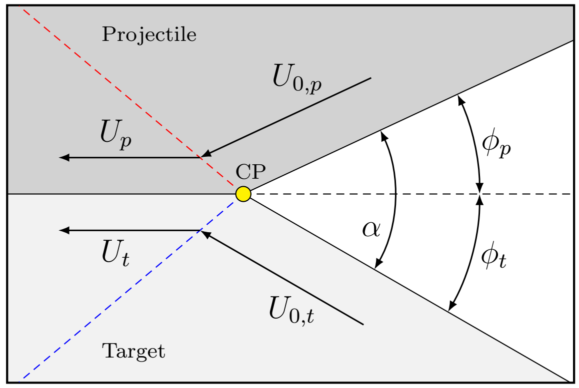

Supplementary Fig. S1: The collision point (CP) frame of reference used in standard jet theory calculations. The effective impact velocities in the projectile and target, $U_{0,p}$ and $U_{0,t}$ respectively give the velocities of material flow into the oblique shocks attached to the collision point (CP). The oblique shocks deflect the material flow along the slip-line interface between projectile and target. The sum of the projectile and target flow deflection angles,ϕ_p and ϕ_t, give the wedge angle subtended by the projectile and target free surfaces, α. The jet is predicted to initiate in the material whose deflection angles meets it critical value first.

A more detailed description of standard theory jetting calculations is given by Kurosawa[45], Vickery[43], Sugita and Schultz[14] and Zhaoxia[13] but a short summary of the procedure used in this work is given here. The geometry used in this analysis is reproduced in Supplementary Fig. S1. The wedge angle subtended by the target and projectile surface during penetration, α, is determined by (1a) where V_0 is the impact velocity, θ is the impact obliquity angle (normal incidence is θ=90°), r_i is the projectile radius, and t is the time after initial impact. In an impact between different materials—the asymmetric case—the deflection angles for the projectile and target sides, ϕ_p and ϕ_t respectively in (1b), sum to the wedge angle.

$$\alpha = \arccos\left(1 - \frac{V_0\, sin(\theta)\, t}{r_i}\right) \tag{1a}$$

$$\alpha = \phi_p\,(U_{0,\,p}) + \phi_t\,(U_{0,\,t}) \tag{1b}$$

Within the frame of reference centered on the collision point, CP, where the penetration projectile surface meets the target surface, the effective impact velocity U_0 in the projectile and target are given by (2a) and (2b), respectively. The effective velocity represents the flow velocity of unshocked material into the oblique shock fronts attached to the collision points.

$$U_{0,\,p} = \frac{V_0\,sin(\theta)}{sin(\alpha)} \tag{2a}$$

$$U_{0,\,t} = \frac{V_0\,sin(\theta)}{tan(\alpha)} + V_0\,cos(\theta) \tag{2b}$$

The relationship between projectile and target is established by the pressure continuity across the material interface, called the slip line. In this case, pressure in the shocked material must be continuous across the slip line (3c) but tangential velocity at the interface may be discontinuous such that material may mathematically slip and the interface. The pressure (3b) in each shocked material is therefore determined by the shocked compression, μ given in (3a), and the specific material properties. It should be noted that a typical linear $U_s - U_p$ relation is used for all projectile and target materials here, where c_0 is the bulk sound speed and s is the slope term coefficient. The values of all material properties are given in Table S1.

Table S1: Mechanical Properties For all Projectile and Target Materials.[55,56]

	2024 Al	6061 Al	304 SS
$\rho_0\,(kg/m^3)$	2784	2703	7890
$c_0\,(m/s)$	5370	5350	4560
s	1.29	1.34	1.49
$\sigma_y\,(MPa)$	345	276	215
$\sigma_u lt\,(MPa)$	483	310	505

$$\mu = \frac{\rho_s}{\rho_0} - 1 \tag{3a}$$

$$P = \frac{\rho\, c_0^2\, \mu(\mu+1)}{(\mu(1-s)+1)^2} \tag{3b}$$

$$P\,(\mu_p) = P\,(\mu_t) \tag{3c}$$

The deflection angle associated with an oblique shock achieving a given compression, μ, is given by (4a). The calculation of the deflection angles for a given wedge angle, α, is accomplished by iterating over a pair of projectile and target deflection angles to find the combination of angles that satisfy the pressure continuity required by (3c).

$$tan^2(\phi) = c_0^2\mu^2 \frac{U_0^2\,(\mu(s-1)-1)^2 - c_0^2(\mu+1)^2}{[\,c_0^2\,\mu(\mu+1) - U_0^2\,(\mu(s-1)-1)^2\,]^2} \tag{4a}$$

$$\frac{d}{d\mu}\,tan^2(\phi)\bigg|_{\mu=\mu_{cr}} = 0 \tag{4b}$$

As previously discussed, the initiation of a jet is predicted to occur when one material reaches it critical deflection angle, or alternately its critical compression, beyond which the associated oblique shock detaches from the collision point, CP, and moves upstream. Shocked material releases into the traction free wedge angle, creating a highly energetic jet of material. The critical deflection angle for a given material experiencing a effective velocity, U_0, can be determined by finding the maximum of (4a). Standard jetting theory therefore postulates that an impact jet initiates when a critical condition is met and $\Delta\phi = \phi_{cr} - \phi = 0$. The value of f, as introduced by Walsh[29], jet velocity in the collisional frame to the effective impact velocity. A value of 1 suggests that the effective impact velocity of the unshocked material is recovered fully in the velocity of the jet. To derive the jet velocity in the lab frame, the motion of the collisional frame (CP) must be considered. For comparison to the values measured by Kurosawa et al[45], the experimental value of f is calculated in (5), which considers the theoretical jet velocity as the average of the ideal projectile and target side jet velocities evaluated at the time of first, critical initiation. This averaging is done because the real, observable jet will have mass contributions from both sides regardless of the theoretical source of initiation.

$$f_{exp} = \frac{2(V_{jet,exp} - U_{0,t})}{(U_{0,t} + U_{0,p})cos(\phi_t)} \tag{5}$$

Thermally Ablative Drag Model

The ablative drag model used in the present work is of the form detailed by Bronshten[49] and implemented by Zhaoxia et al[13]. It represents the classical model of thermal ablation commonly applied to meteor ablation in planetary atmospheres, and thermalizes a fraction of the flow energy dissipated in the drag of the particle to vaporize material and reduce the particle mass.

The general equation of motion (6a), mass ablation (6b), and particle luminosity (6c) are given below, where the particle mass is m, the free-stream velocity is V, and the particle cross-sectional area to the flow is A_c. The drag coefficient (C_d), ambient atmosphere density (ρ_{atmo}), heat transfer coefficient (Λ), and heat of ablation (Q) are assumed to be constant. The heat transfer coefficient (Λ) is the fraction of the kinetic energy of the oncoming stream that contributes to ablation of particle mass, and the heat of ablation (Q) is taken as the energy per unit mass to raise the temperature and vaporize an initially molten particle, assumed to have been melted during the jetting process. The coefficient of radiative efficiency (γ_0) is assumed to be constant for all ablating particles, and is therefore incorporated only as a normalization constant for the particle luminosity, I.

$$m\,\frac{dV}{dt} = -\frac{1}{2}C_d\,\rho_{atmo}V^2 A_c \tag{6a}$$

$$\frac{dm}{dt} = -\frac{1}{2}\frac{\Lambda}{Q}\rho_{atmo}V^3 A_c \tag{6b}$$

$$\frac{I}{\gamma_0} = -\frac{1}{2}\frac{dm}{dt}V^2 \tag{6c}$$

The assumption of spherical particle shape leads to the self-similar velocity dependent solution (7a) for particle radius (r) assuming an initial radius (r_0) and initial velocity (V_0). The governing equations are rewritten assuming spherical particle shape with constant density (ρ_{frag}) in (7b) and (7c). The ablation parameter K heavily determines the ablation and drag behavior of the particle. The assumption of thermal ablation may not be appropriate for the mass loss under the experimental conditions discussed, but this basic ablative drag model offers a good starting point and is sufficient to demonstrate and evaluate the nature of of a particle based flash mechanism.

$$r(t) = r_0\,e^{-K(V_0^2 - V(t)^2)} \tag{7a}$$

$$\frac{dV}{dt} = -\frac{3}{8}\alpha_0 V^2\,e^{-K(V^2 - V_0^2)} \tag{7b}$$

$$\frac{dm}{dt} = 4\pi r^2 \rho_{frag}\frac{dr}{dt} \tag{7c}$$

$$K = \frac{1}{6}\frac{\Lambda}{Q\,C_d} \tag{7d}$$

$$\alpha_0 = \frac{C_d\,\rho_{atmo}}{r_0\,\rho_{frag}} \tag{7e}$$

Table S1: Thermal Ablation Model Parameters. Only 2024Al projectiles impacting 6061Al targets were analyzed with the model , so the mixed material nature of the jet in other configurations was not considered.

ρ_{frag}	2375 kg/m^3	Λ	0.9
Q	13500 (kJ/kg)	C_d	2

Particle Cloud Self Occlusion

The effect of particle self-occlusion must be considered under the assumption of a particle ablation driven impact flash. From the viewing perspective of a detector, a large fraction of the total particle radiant intensity may be block from view by other particles in the early, dense particle cloud. Here, we seek to estimate the effect of this occlusion by evaluating the fraction of particle surface area that is visible from a single perspective. To approximate a generalized particle cloud representing an impact flash we volumetrically expand a initial randomly packed sphere of particles following a prescribed size distribution. The number of particles particles participating in the impact flash is estimated assuming 5% of the projectile mass participating in the jet, based on prior work in the field. The very large number of particles implied by this jet mass requires a scaled calculation to be made. An exponential distribution in particle volume is assumed, and the calculation initial configuration is generated by the MATLAB based random-sphere-packing algorithms provided by Black and Cheviakov[57]. The resulting initial packed configuraiton of particles is shown in Fig. S4a. The packed particle sphere is expanded volumetrically. The visible, non-overlapped fraction of particle surface area is calculated by Monte Carlo sampling of the projected particle surface areas projected on the y-z plane. Here, the view of the hypothetical detector is directed along the x-axis.

The calculation result for visible area fraction is shown in Fig. S4b. The shape is very well fit by exponential decaying towards full visibility. Some fraction of the initial area is of course visible to the detector at the start, given by f_0. This exponential shape is not unexpected. Grady[58] identified the applicability of Johnson-Mehl crystal growth dynamics to the problem of estimating fragment statistics experimentally in dense debris clouds. The random initial packing and volumetric velocity field resembles the growth of randomly nucleated circular crystals in the y-z plane, if the cloud is followed backward in time. Rather, starting at a large times where the particle cloud is diffuse and moving back in time, the particles appear to grow in relation to the cloud dimensions, eventually overlapping each other in the projected view. The overlapped area is analogous to the extended volume identified in the Johnson-Mehl model. The time behavior of the occlusion ratio, f_{occ}, is then characterized by the time constant, τ_{occ}.

The calculation must be scaled up to reflect the actual condition of the impact flash. The following scaling relations were developed to estimate the effective occlusion time constant, τ_{occ}, under experimental conditions by scaling a calculated, reference occlusion time constant fit in Fig. S4b, $\bar{\tau}$. Assuming the an initial spherical mass of diameter D is divided into fragments of diameter d, the number of fragments, N, goes as (8b). If those fragments are expanded, forming our impact flash, such that no particles are self-occluded from a single perspective, then the minimum projected flash area accomplishing this goal will be the sum total of the particle projected areas. This minimum, no occlusion, cloud radius is identified as R_* in (8a).

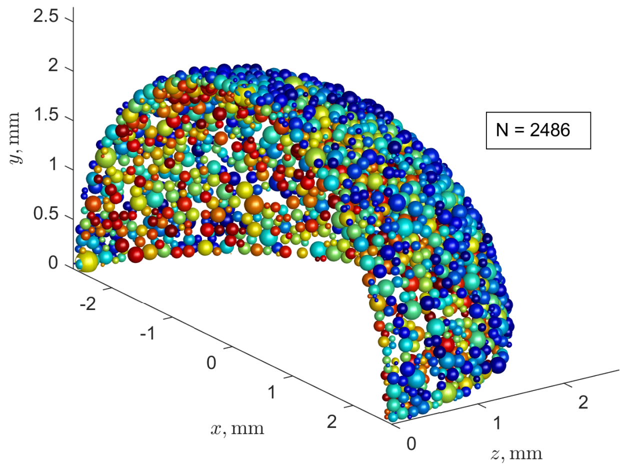

(a) Scaled Calculation Particle Initial Configuration

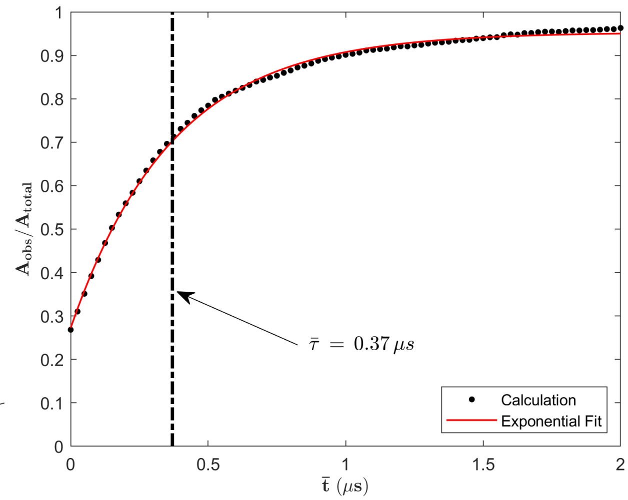

(b) Scaled Occlusion Area Ratio

Supplementary Fig. S2: The initial reference particle configuration consisting of randomly packed spheres is shown in (a). A linear radial velocity profile is applied to the particles in the shell, with the outermost particles traveling at the observed jet velocity (10 km/s) and the innermost at the impact velocity (3 km/s). The initial calculation configuration represents a shell of jetted particles originating at the projectile surface, distributed exponentially in particle volume with an average diameter of 110 , comprising a jetted mass of 5% the projectile total mass. The observable particle surface area viewable from the the detector (viewing along -x direction) is calculated via monte carlo sampling of the non-overlapping area projected on the Y-Z plane. The ratio of observable surface area to total projected particle area (sum total of circular particle area in Y-Z plane) for the expanded calculation cell (b) is fit using and exponential form (9a) and the resulting time constant is scaled according to (9c). The resulting occlusion ratio function (9a) roughly approximates the fraction of total radiant luminosity emitted from the surface of spherical particles that is visible to the detector in an expanding ablating particle cloud.

The timescale associated with this no occlusion condition is given by t_*, where V is the expansion velocity of the particle cloud boundary. This suggests that the timescale associated with full visibility for all the participating N fragments, for a given configuration and expansion velocity field, should scale roughly as the 1/6 power of the number of fragments, holding the expansion velocity of the cloud and the initial volume of participating mass constant.

$$R_*^2 \propto N d^2 \tag{8a}$$

$$N \propto (\frac{D}{d})^3 \tag{8b}$$

$$t_* = R_*/V \simeq \frac{D}{V}\sqrt{\frac{D}{d}} \simeq \frac{D}{V}\,N^{1/6} \tag{8c}$$

$$\tag{8d}$$

As such, the occlusion time constant in the exponential form given by (9a) should scale as shown in (9b), and can be estimated for the experimental configuration using a calculated reference as shown in (9c). Note, the reference values apply to calculated configuration shown in Fig. S4a, with for example, $\bar{N} = 1659$. For the reference configuration shown, the initial packed configuration radius, $\bar{R_0}$, and expansion velocity $\bar{V}$, are chosen to reflect the experimental geometry and jet velocity such that the first two terms in (9c) are 1. The size distribution of fragments therefore determines N, where a large enough fragment size was chosen for the reference calculation to make $\bar{N}$ computationally practical. The experimental value of N is estimated using the experimentally determined fragment sizes discussed in the main body of the paper.

$$f_{occ} = (1 - f_0)(1 - e^{(-t/\tau_{occ})}) + f_0 \tag{9a}$$

$$\tau_{occ} \propto \frac{R_0}{V} N^{1/6} \tag{9b}$$

$$\frac{\tau_{occ}}{\bar{\tau}} \simeq (\frac{R_0}{\bar{R_0}})(\frac{\bar{V}}{V})(\frac{N}{\bar{N}})^{1/6} \tag{9c}$$

Extension to Oblique Impacts

The mechanics of jetting, material ejection, and crater excavation all remain consistent in the case of oblique impact—where the projectile velocity vector is not normal to the target plane—but the general axisymmetry of the flash and ejecta cone is broken. General bilateral symmetry about the plane formed by the projectile impact velocity vector and the target plane normal is retained. We only consider 45° impact obliquity here; the 45° oblique configurations for both SS/Al and Al/Al are given in Supplementary Figs. S3 and S4, respectively.

In these configurations, the projectile has considerable momentum along the target plane surface. As a result, there is much more material excavated and ejected in the direction of the projectile's travel along the surface (+y direction) and there is corresponding asymmetry in the ejecta cone. This momentum also affects the jetting behavior and therefore the impact flash. The relative lateral motion of the projectile along the target plane affects the effective impact velocities $U_{0,p}$ and $U_{0,t}$ in the collision point frame of reference (given by supplementary equations ($2a$) and ($2b$) respectively) and therefore the jetting behavior of the system. Each point in the projectile contact locus (ring of contact points), experiences a different effective velocity and the jets developed there will initiate and evolve differently, but jets will form around the entirety of the contact locus. This behavior can be seen in the front view images of Figs. S3a-b and S4a-b, as radiating material is initially jetted in all directions around the penetrating projectile. The inclined shape of the impact flash in side profile is determined by the altered set of trajectories achieved by this non-axisymmetric

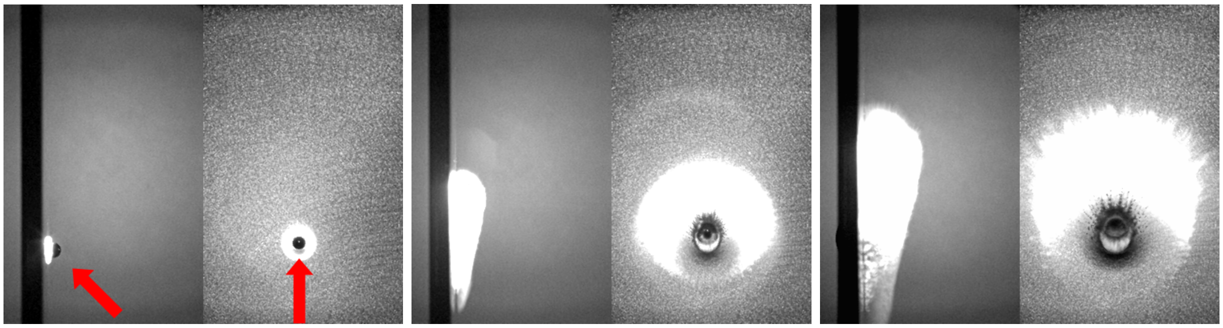

(a) $t = 0.2\,\mu s$ (b) $t = 2.2\,\mu s$ (c) $t = 4.4\,\mu s$

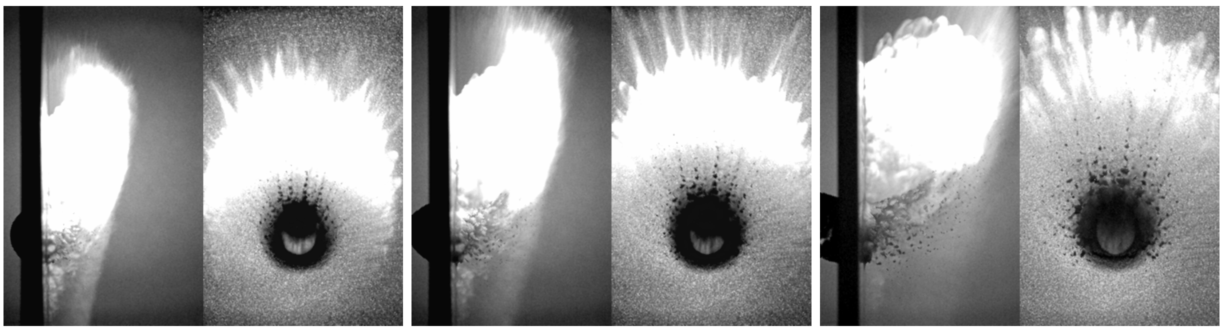

(d) $t = 6.8\,\mu s$ (e) $t = 9.2\,\mu s$ (f) $t = 13.6\,\mu s$

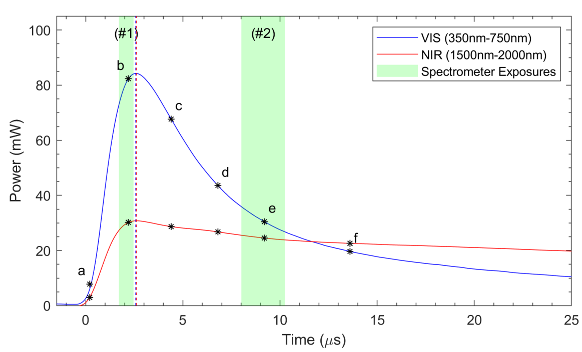

(g) Visual and Near-IR Luminosity

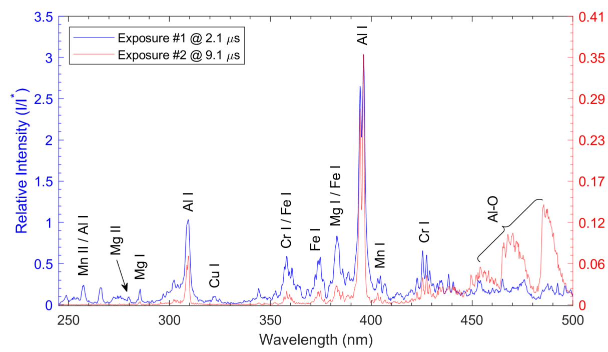

(h) UV-Visual Gated Spectra (250-500nm)

Supplementary Fig. S3: 304SS projectile impacting 6061Al target at 45°obliquity with velocity of 3.0 km/s in 15 Torr air. See Fig. 2 for description of figure elements.

jetting behavior.

The concentration of high velocity ejected particles in the direction of projectile motion leads to a very intense flash in the +y direction for the duration of the experiments and visible dark ejecta rays emanating from the crater in front view images at later times (d-f). The transit of the ablated vapor cloud boundary by solid fragments is readily observable in these impacts, creating rays and bright streaks on the leading edge of the flash as ejected particles entrain radiating gas in their wake. The peak VIS luminosity is largely similar between normal and oblique impacts, but the NIR peak luminosity is greatly increased under oblique conditions. In all cases, the total observed emitted VIS and NIR energy is much greater. Additionally,

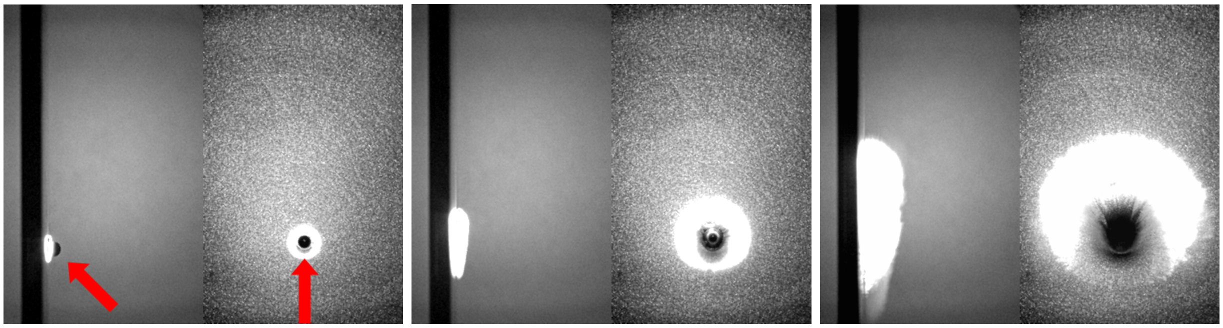

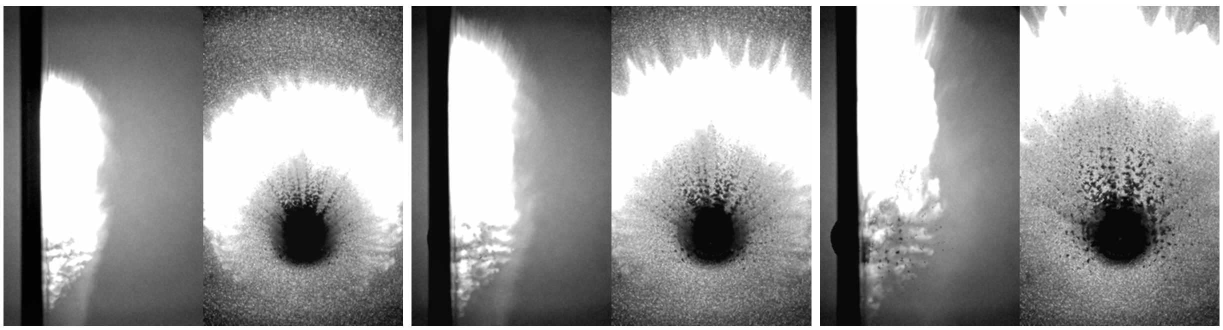

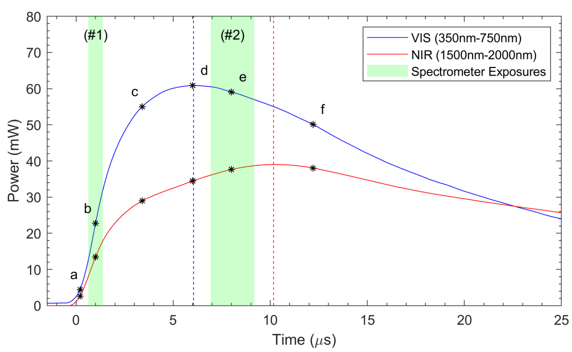

(g) Visual and Near-IR Luminosity

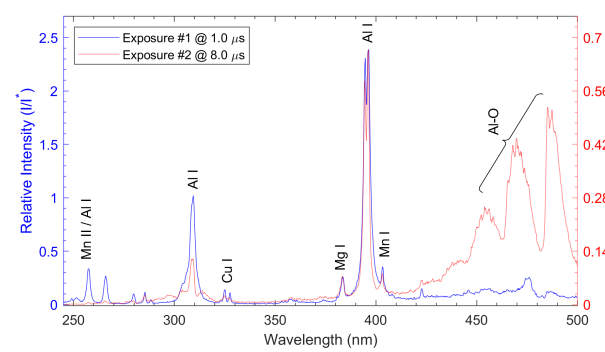

(h) UV-Visual Gated Spectra (250-500nm)

Supplementary Fig. S4: 2024Al projectile impacting 6061Al target at 45°obliquity with velocity of 3.1 km/s in 15 Torr air. See Fig. 2 for description of figure elements.

the early time oblique emission spectra in Fig. S3 shows higher relative intensities of 304SS species peaks to 6061Al species peaks than the normal impact for the SS/Al configuration (Fig. 2). This may be an indication of higher relative participation of projectile material in the composition of the impact jet, as would be predicted at higher impact obliquity[14,44,52,59], but the variation in exposure timing between experiments renders direct comparison uncertain.

The 45° obliquity Al/SS impact (Fig. S5) displays somewhat bizarre behavior as the downrange edge (+y) of the shallow ejecta cone appears to extend back to the target surface before curving back away uprange (d-f). This distinct shape gives the visual impression of the ejecta somehow impacting the target

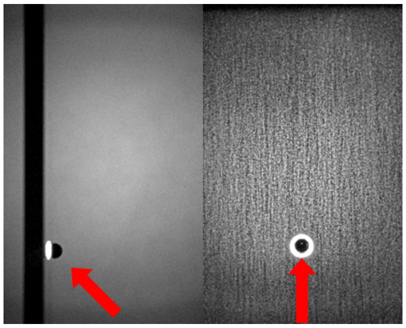

(a) $t = 0.2\ \mu s$

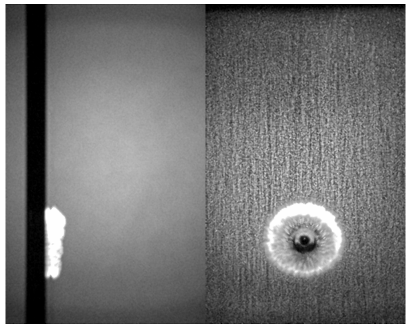

(b) $t = 1.2\ \mu s$

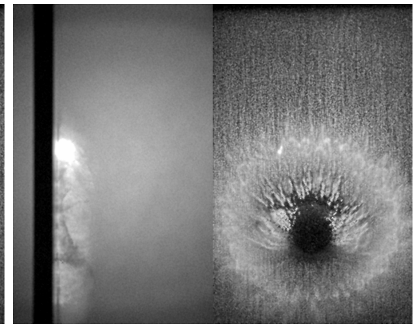

(c) $t = 4.2\ \mu s$

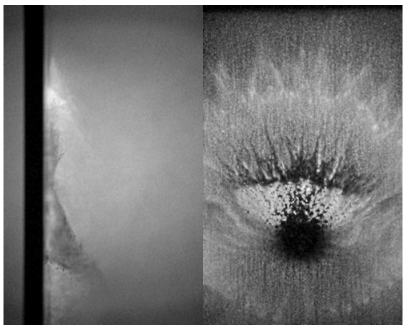

(d) $t = 7.2\ \mu s$

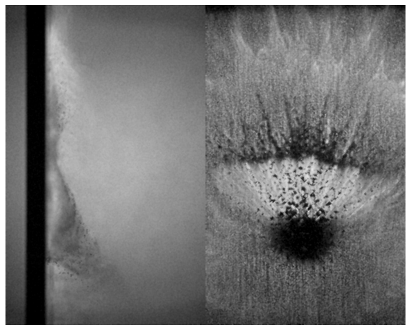

(e) $t = 10.0\ \mu s$

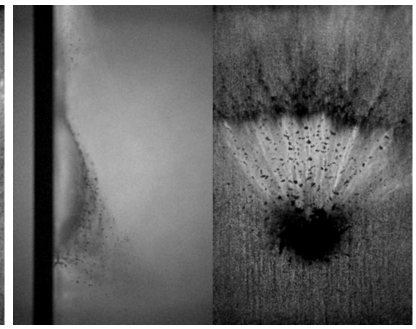

(f) $t = 15.2\ \mu s$

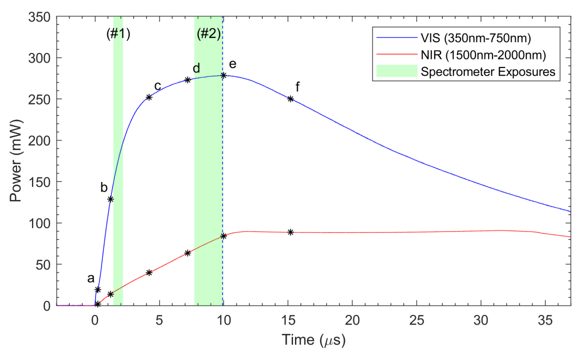

(g) Visual and Near-IR Luminosity

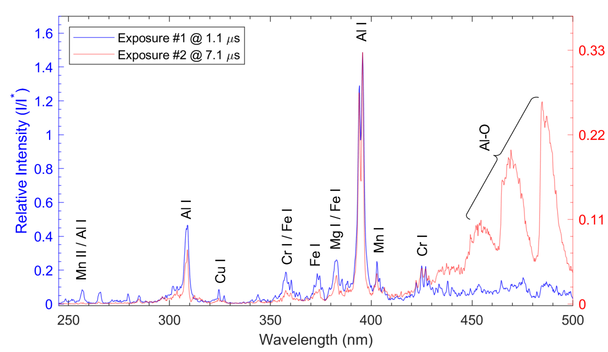

(h) UV-Visual Gated Spectra (250-500nm)

Supplementary Fig. S5: 2024-Al Projectile Impacting 304SS Target at 45°Obliquity with Velocity of 3.0 km/s in 15 Torr Air. See Fig. 2 for description of figure elements.

surface and bouncing off; this is, of course, not accurate. Rather, the generally monotonic expected sweep of trajectories from shallow to steep seems to be interrupted, ”skipping” back to shallow and slower solid fragment trajectories produced during the generation of the primary ejecta cone. The observed peak VIS luminosity in Fig. S5g is roughly 90% higher than that of the normal impact. NIR luminosity is substantially increased (g) over the corresponding normal impact, likely by a similar fraction as VIS, but in this single case the detector saturated shortly after time (e) unfortunately making it difficult to assess magnitudes and NIR peak time. In both normal and oblique Al/SS impacts, the luminosity magnitude is so large that the decay is much slower than other configurations. Flash intensity in both bands persist long enough that issues with the observable extent of the expanding cloud, or even secondary impacts of high velocity fragments in the test chamber may affect the data at longer times. However, similar to Fig. 5, the flash outruns the boundary of the the inclined ejecta cone in Fig. S5(c), and the shape and extent of the flash zone bears little visual correlation with that of the solid ejecta cone. Once again, the smooth continuity between flash boundary and ejecta cone boundary that is observed for all SS/Al and Al/Al configurations is not seen when Al impacts SS. The smooth variation of ejected particle trajectories required to generate flash/ejecta boundary continuity implies some measure of continuity in the mechanisms generating ”hot” flash material and ”cold” ejecta fragments. The absence of boundary continuity in Al on SS impacts therefore implies discontinuous behavior between jetting and main ejecta formation mechanisms.